Modeling Energy and Carbon Fluxes in a Heterogeneous Oak Woodland: A Three-Dimensional Approach

Hideki Kobayashi[1,5], Dennis Baldocchi[1], Youngryel Ryu[2], Qi Chen[3], Siyan Ma[1], Jessica Osuna[1], Susan Ustin[4]

1. Department of Environmental Science, Policy and Management, University of California, Berkeley, Berkeley, 94720, CA
2. Department of Organismic and Evolutionary Biology, Harvard University
3. Department of Geography, University of Hawai'i
4. Center for Spatial Technologies and Remote Sensing, University of California, Davis
5 Research Institute for Global Change, Japan Agency for Marine-Earth Science and Technology

Abstract

Most land surface and ecosystem models assume that a vegetated canopy can be abstracted as a turbid medium when such models compute mass, energy, and carbon exchange. However, those models fail to simulate radiation environments in heterogeneous landscapes. This study aims to couple a spatially explicit three-dimensional (3D) shortwave and longwave radiative transfer model with a soil and canopy energy balance and canopy physiology model (CANOAK-FLiES), to investigate how well the 3D model performs in a heterogeneous landscape compared to a 1D model. The canopy structural parameters were extracted using airborne-based Light Detection And Ranging (LiDAR) data and digital cover photographs. The developed model was compared with a wide variety of field and remote sensing data (e.g., hyper-spectral remote sensing images, overstory and understory radiation, and tower-based energy and CO_2 fluxes) in a woody oak savanna in California. Overall, the simulated spatial and diurnal patterns of the radiation environment were consistent with the measurements of shortwave and longwave wavebands. The 3D approach worked better than the 1D approach from the wet mild spring to the dry hot summer while the relative importance of using the 3D approach depends on climate and canopy physiological conditions as well as the canopy structure. With low leaf area index in the oak woodland, the woody elements absorbed 12%-39% of the PAR and 20%-52% of the NIR radiation. Consequently, 12% of the daytime energy flux was used as woody heat storage at our study site. This novel 3D model has the potential to serve as a useful tool for analyzing the spatio-temporal variability of radiation and energy fluxes in evaluating footprints of radiation sensors and eddy covariance fluxes, and serve as a standard in evaluating the performance of a hierarchy of simpler land surface models to compute mass and energy exchange of heterogeneous landscapes.

1. Introduction

Most land surface and ecosystem models assume that a vegetated canopy can be abstracted as a turbid medium to compute mass, energy, and carbon exchange. With this assumption, the canopy is horizontally homogeneous as leaves are randomly distributed in space. Consequently, radiation only changes in a vertical direction. This simplified modeling makes it difficult to evaluate the radiation environment in spatially heterogeneous landscapes such as savanna ecosystems (Sankaran et al., 2005; Scholes and Archer, 1997). In particular, the spatial separation of individual tree crowns forms regions where beams of light travel without interactions with foliage and regions where light is strongly attenuated. This neglected spatial attribute in the turbid medium type models motivates us to challenge and critique the widely held assumption of a turbid medium. We aim to take a spatially explicit three-dimensional (3D) approach to understand the role of heterogeneous structure on the energy and carbon fluxes. The 3D approach requires more computation time and canopy structural variables than 1D turbid medium models. However, the 3D approach is expected to give more reliable energy and carbon fluxes when the reliable canopy structural variables are available. Also, airborne- Light Detection and Ranging (LiDAR) data has been retrieved in many areas, thus it is expected more LiDAR data would be available in the near future. Therefore, the 3D model can fill the theoretical gap between 1D models and actual ecosystems, and can be used to investigate where and when the simplified models give a large error to simulate the radiation (Widlowski et al., 2011), energy and carbon fluxes. The central questions asked in this study are as follows (1) How can we model the landscape scale spatial variability of radiation and energy budgets in heterogeneous ecosystems (not only shortwave radiation but also longwave radiation and net radiation)? (2) How can we compare the simulated radiation quantities with irregularly placed measurements in time and space? and (3) How well does the 3D approach perform in a heterogeneous landscape compared with the 1D approach?

For the computation of 3D radiation environments and energy exchanges in heterogeneous landscapes, the model is required to simulate visible, near infrared (NIR), and thermal infrared radiation (TIR). Current 3D radiative transfer and energy exchange models have been mainly concentrated on the beam dominant spectral domain

(photosynthetically active radiation, PAR), while highly scattered NIR and TIR domains tend to be simplified (Cescatti, 1997a; Gutschick, 1990; Medlyn, 2004; Norman and Welles, 1983; Sinoquet and Bonhomme, 1992; Sinoquet et al., 2001; Wang and Jarvis, 1990), which makes it difficult to compare the spatial radiation environments with measurements. Another class of 3D models considers scattered and thermal emission within the radiative transfer scheme in greater detail (Gastellu-Etchegorry, 2008). However, this class of models does not consider the energy exchange that is associated with and controlled by plant physiology, like transpiration and stomatal conductance. Nor have these models been well tested on vegetation canopies. In this study, we continue to work on a 3D radiative transfer model, the Forest Light Environmental Simulator (FLiES) (Kobayashi and Iwabuchi, 2008). For the simulation of energy and carbon exchange, we combine the CANOAK scheme (Baldocchi, 1997; Baldocchi and Meyers, 1998; Baldocchi and Harley, 1995; Baldocchi and Wilson, 2001) with the 3D radiation scheme of FLiES.

Testing model results is always a challenge, especially when the model is designed to focus on details. The radiative transfer models have been tested by the model intercomparison approach (Pinty et al., 2001; Pinty et al., 2004; Widlowski et al., 2007; Widlowski et al., 2011) or by different sources of field data, such as bidirectional reflectance (Malenovsky et al., 2008; North, 1996), transmittance measurements (Law et al., 2001; Norman and Welles, 1983; Sinoquet et al., 2001; Tournebize and Sinoquet, 1995; Wang and Jarvis, 1990), and gap fraction measurements (Cescatti, 1997b). However, these field data are usually very limited. To achieve the goal of this study, we need a study site that has firsthand data suitable for 3D model validation.

We conducted this model evaluation study in a heterogeneous oak woodland in California. This site is suitable because it was established for eddy covariance measurements of energy and CO_2 fluxes in 2001 and over the intervening years a large body of plant physiological, canopy structure and remote sensing data on the canopy's functional and structural attributes have been collected. For example, two scenes of airborne-based LiDAR data were collected and are used to extract tree shapes and spatial patterns (Chen et al., 2006). In addition, a traversing radiometer system, which measures the radiation along horizontal transects, allows us to compare the simulated

116 spatial variations in understory radiation environment with these field measurements
117 (Gamon et al., 2006; Ryu et al., 2010a). Airborne Visible/Infrared Imaging
118 Spectroradiometer (AVIRIS) data were collected to produce information on
119 hyperspectral reflectance across the spatial domain of the woodland.
120
121 The objectives of this study are (1) to couple a three dimensional radiative
122 transfer model with a soil and canopy energy balance and a canopy physiology model
123 (CANOAK-FLiES), (2) to test the overall performance (spatial patterns of radiation and
124 energy fluxes) of the 3D model, and (3) to compare the energy and carbon fluxes
125 simulated by the 3D approach with the 1D approach that is built from simple turbid
126 medium slabs layered on the landscape. We show how the energy and the carbon fluxes
127 are governed by the radiation partitioning in the heterogeneous landscape. First, we
128 extended FLiES to the TIR domain to simulate spatial patterns of net radiation, based on
129 leaf temperature information derived from the energy balance model. Second, we
130 develop the CANOAK-FLiES model by combining the extended 3D radiative transfer
131 model, FLiES (Kobayashi and Iwabuchi, 2008) and the soil/canopy energy balance and
132 canopy physiology model, CANOAK (Baldocchi and Meyers, 1998). Third, we
133 compared the model outputs with various field measurements. To perform the
134 comparison, we collected most of the model input variables (tree structural, optical, and
135 photosynthesis parameters, and soil parameters) from field measurements and airborne
136 LiDAR data.
137
138

2. Model description

To run the model, we created heterogeneous woodland landscapes and forced a periodic boundary condition at the four lateral spatial boundaries. Tree positions and their crown diameters were explicitly defined from field and remote sensing measurements. We modeled individual crowns using spheroid shapes with two domains (Figure 1a); outer domain was occupied by randomly distributed leaves and inner domain was occupied by randomly distributed woody elements. Heights and diameters of inner domains were set to 75% of crown dimensions. We assumed the constant leaf and woody area densities (m^2 m^{-3}) over the all crowns. Stems were modeled as cylinders. The model can also be run in one dimension (1D) by layering the simple slabs to the height of 11 m on the surface (Figure 1b). In the 1D model, the woody elements can be considered assuming that the all woody elements are randomly distributed within the layer. We used this simple 1D scheme for the comparison with the 3D scheme.

2.1 Radiative transfer model

FLiES was originally a shortwave radiative transfer model in 3D landscapes (Kobayashi and Iwabuchi, 2008). Radiative quantities needed for energy and carbon exchange simulation (e.g. albedo, transmission, and absorption) were simulated by a Monte Carlo ray tracing method. FLiES is capable of simulating exact higher-order photon scattering under the heterogeneous landscape created by 3D tree objects as defined in Figure 1a. In this study, we did not use the atmospheric radiative transfer module and photons were fired at the top of the landscape. The initial positions of the photons were randomly chosen across a two dimensional domain at the top of the landscape, and incoming directions of these photons were randomly determined for isotropic diffuse radiation and set to the sun direction for the beam radiation. When the photons intersected the crowns, we determined the photon path length inside the crowns. The photon path lengths and the scattering directions were determined by random numbers followed by a probability distribution function of Lambert-Beer's law and a scattering phase function. These processes continued until the photon exited from the crown. On stems and the soil surfaces, the photon was reflected. This ray tracing continued until the photon exited from the simulated landscapes.

The radiation absorbed by the leaves and woody elements was calculated at every scattering event. The downward and upward radiation fluxes at the top of the landscape and at the understory level were calculated by summing the photons that passed through the horizontal plane at those levels. Bidirectional reflectance was calculated by the local estimation method, which samples the reflectance contributions at every scattering event (Antyufeev and Marshak, 1990; Marchuk, 1980).

While FLiES is a radiative transfer model for shortwave radiation, we extended the model to the longwave portion of the electromagnetic spectrum. In longwave domain, there are thermal emission sources inside the landscape such as leaves, woody elements, and the soil surface. These emissions should be considered as well as the incoming radiation from the sky. The ray tracing scheme in the TIR domain is similar to that of the solar domain. In TIR, optical properties of leaves, woody elements and the ground surface were characterized by their emissivity (ε). These reflectances were calculated from ε, ($\rho = 1 - \varepsilon$) according to Kirchhoff's law. Transmittance of leaves was assumed to be zero. Scattering directions of photons were determined by the same method in the solar domain. The locations $\mathbf{r} = (x, y, z)$ and directions $\Omega_E = (\theta_E, \phi_E)$ of photon emissions from leaves, woody elements, and the soil were determined by a 3D emission probability distribution function (P_E), where P_E is a function of temperature distribution in the plant canopy. The details of the derivations of P_E, emission position and direction are described in Appendix B.

We fired 2.0 x 10^7 photons for each spectral domain (PAR, NIR, and TIR) at hourly time steps. The number of photon was determined by preliminary runs of the 3D model. We confirmed that the computations with this number of photon provided a steady state radiation and energy fluxes. The size of simulated landscape was set at 100 m^2. In this study, the sampling grid of all simulated variables was set at a 1 m^3 volumetric pixel (voxel). The average input photon density at the top of the canopy was 6000 per sampling grid (1 m^2). The spectral bidirectional reflectances were simulated at the AVIRIS overpass times. For this simulation, the size of the simulated landscape was set at 600 m^2 and the sampling grid was set at 3.2 m^2, which is close to the AVIRIS pixel size. For spectral bidirectional reflectance simulation, we fired 2.0 x10^8 photons

for each AVIRIS spectral band. The average photon density at the top of the canopy was 5719 per sampling grid (3.2 m^2).

2.2 Incorporation of energy exchanges

To simulate energy exchanges between the atmosphere and the canopy, we employed an energy and carbon exchange model, CANOAK (Baldocchi, 1997; Baldocchi and Meyers, 1998; Baldocchi and Harley, 1995; Baldocchi and Wilson, 2001). The model simulates fluxes such as sensible heat (H, Wm^{-2}), latent heat (λE, Wm^{-2}), photosynthesis (P_s, μmol m^{-2} s^{-1}), and soil heat flux (G, Wm^{-2}) at hourly time steps. The input variables for the CANOAK model includes air temperature (^oC), shortwave radiation (W m^{-2}), total and diffuse PAR (μmol m^{-2} s^{-1}), water vapor pressure (kPa), wind speed (m s^{-1}), CO_2 mixing ratio (ppm), soil moisture (m^3 m^{-3}), atmospheric pressure (mb), and incoming TIR. All parameters except for soil moisture were variables at the top of canopy. In the CANOAK-FLiES, we used the same input variables. We ignored the spatial variability of the soil moisture and used the same variable across the ground pixels.

We adapted the CANOAK's energy and physiology scheme to individual tree voxels (1 m^3) or ground surface pixels (1 m^2). The energy fluxes and photosynthesis were simulated with each tree voxel or ground surface pixel. Landscape scale energy and carbon fluxes were then obtained by summing all local fluxes. For the turbulence scheme, we employed the 1D Lagrangian random walk model (Thomson, 1987) and the dispersion matrix concept of Raupach (1988) that are used in the original CANOAK model. Aggregating the local energy and carbon fluxes horizontally for every 1 m vertical level, the vertical profiles of the fluxes were prepared and were used to run the 1D turbulence model. The fluxes on leaves and the soil were calculated by the energy budget equation.

$$R_{abs} - \sigma\varepsilon T^4 - H - \lambda E - G = 0 \quad (1)$$

where, R_{abs} is the sum of absorbed shortwave (PAR and NIR) and longwave (TIR) radiation, and G is the soil heat flux. G is zero on the leaf surface.

$$R_{abs} = R_{PAR} + R_{NIR} + R_{TIR} \quad (2)$$

The fractions of the sunlit and shaded leaf area densities in each voxel were computed by the Monte Carlo ray tracing together with other radiative quantities. While doing the Monte Carlo ray tracing, we counted the number of scattering events that photons first hit leaves. The fraction of the first order scatterings to all scatterings is related to the projected sunlit leaf area density to the sun direction. The sunlit leaf area density was calculated by dividing the projected sunlit leaf area density by the mean leaf projection function in the sun direction. The details are described in Kobayashi and Iwabuchi (2008). The energy balance and photosynthesis were separately simulated for the sunlit and shaded leaves. Shaded leaves only received diffuse sky radiation and scattered radiation in the canopy. Sunlit leaves received the direct solar radiation as well as diffuse sky and scattered radiation.

The leaf temperature (T_l) and the soil surface temperatures (T_s) were simulated by the second-order approximation of the energy budget equation (Paw U, 1987). The simulation of the equation (1) and TIR radiative transfer were continued in an iterative manner until a convergence of the radiation and energy flux fields over the landscape was found (Figure 2). Stomatal conductance of the leaf surfaces was simulated by the Ball-Berry equation (Ball, 1988), in which stomatal conductance was solved as an interdependent relationship between leaf photosynthesis and stomatal conductance. An analytical approach was employed to solve this interdependent relationship (Baldocchi, 1994). G was calculated by the soil heat transfer scheme of Campbell (1985).

The original CANOAK did not have an energy balance module on the woody elements. We treated the woody surface energy balance in the same manner as we did the soil surface. The woody (branches and stems) heat storage was simulated by the Force-Restore method (Haverd et al., 2007; Silberstein et al., 2003; Watanabe and Ohtani, 1998). For the energy balance simulation in woody elements, we employed “a big wood” approach. The absorbed radiation in each voxel was first summed over the landscape. Then the energy balance and woody storage were computed.

3. Methods and data

3.1 Study site

Our study site is an oak woodland located in the foothills of the Sierra Nevada in California, USA (Figure 3, Tonzi Ranch: 38.4318 N, 120.9668 W, elevation: 177 m). The site experiences a Mediterranean climate with dry hot summers and mild winters (Baldocchi et al., 2004; Ma et al., 2007). The percentage of tree cover across the landscape is 47% (Chen et al., 2008). Deciduous blue oaks (*Quercus douglasii*) dominate the site. Some gray pine trees (*Pinus sabiniana*) are present, but they constitute only a small portion of the stand (<10%) (Ryu et al., 2010a). The woodland understory is covered by cool-season C3 annual species, including *Brachypodium distachyon L., Hypochaeris glabra L., Trifolium dubium Sibth., Trifolium hirtum All., Dichelostemma volubile A., and Erodium botrys Cav* (Ma et al., 2007). Vegetation at our study site is highly clumped and most of the clumping effect is considered to attribute to the spatial scale larger than the crowns (Ryu et al., 2010a; Ryu et al., 2010b). The element clumping index and the maximum tree LAI at the study site are 0.49 and 0.77, respectively (Ryu et al., 2010a). Budburst normally occurs in March, and the LAI reaches maximum at the end of April or the beginning of May.

3.2 Data collection

To test the model, we defined three areas: No. 1, 2, and 3 (Figure 3). The size of area No. 1 is 600 by 600 m. This includes most of the daytime footprints of the eddy covariance measurements (Kim et al., 2006). Area No. 2 includes the flux tower location in its center position, and area No. 3 includes the location of the traversing radiometer system. Both No. 2 and 3 are 100 by 100 m. We compared simulated canopy reflectance (nadir-view spectral bidirectional reflectance factor) with airborne remote sensing data at area No. 1. The radiation budget and energy flux measurements at the top of the oak canopy were compared to area No. 2. At area No. 3, we simulated the spatial patterns of the radiation environments and compared them with understory radiation measurements (downward and upward PAR, net radiation, and spectral transmittance) along the 20 m traversing radiometer system and along two 26 m

transects (Transects A and C).

3.2.1 Spatial structure of the woodland

Input data sets are summarized in Tables 1 and 2. For the photosynthesis and stomatal conductance module, we used the maximum photosynthetic capacity (V_{cmax}) measured by Xu and Baldocchi (2003). Other physiological parameters we used are the same as Chen et al. (2008). Tree positions, heights, and crown radii at the study site were extracted from LiDAR observation (Optech ALTM 2025). The LiDAR data were collected for the study area on April 20, 2009. The sensor recorded the first and last return pulses. The scanning pattern was z-shaped. The scanning angle was 15 degrees, and the flying altitude was about 900 m, corresponding to a swath of about 500 m. The average horizontal GPS solution difference from two base stations was 10-15 cm. The vertical accuracy was -0.01 ± 0.05 m, based on the comparison of 819 test points and interpolated digital elevation model elevations. The footprint size was about 18 cm. The average posting density was 4.1 points per square meter, resulting in an average spot spacing of about 0.5 m. The individual tree crowns were delineated using the Toolbox of Lidar Data Filtering and Forest Studies (Chen, 2007), which generates digital elevation models using morphological methods (Chen, 2009; Chen et al., 2007) and separates individual trees using watershed-segmentation algorithms (Chen et al., 2006). To identify individual trees, a digital surface model of 1 m cell size was first interpolated from the maximum laser height within individual cells; then the digital elevation model was subtracted from this to generate a canopy height model on which trees are segmented. The tree isolation results are refined by visual interpretation of the canopy height model and field survey. In area No. 3, it was necessary to determine positions, heights, and crown radii accurately for the comparison of the simulated results with radiation measurements along the transects (Figure 3). Therefore, we extracted individual tree positions and crown radii by visual interpretation of the digital height model and the field survey.

3.2.2 Canopy structure

For tree leaves, we chose an erectrophile leaf inclination angle function based

on measurements conducted at the same site (Ryu et al., 2010a). For grass leaves and branches we assumed erectrophile and spherical functions, respectively. Leaf and woody area densities in the crowns were derived by gap fraction measurements along the seven transects (Figure 3). The gap fractions were measured by digital cover photography (DCP) (Macfarlane et al., 2007; Ryu et al., 2010a). We took photographs with a digital camera (RICHO R8) at the zenith direction at 1 m intervals on August 5, 2009 (the full leaf period) and on January 11, 2010 (the leafless period). We extracted only the portion of the images near the zenith direction (0 to 18 degrees from the zenith). All images were converted to black and white images by applying thresholds to the blue-band histogram, and gap fractions were computed from fractions of black (leaf and woody) pixels. The leaf and woody area densities of the crowns were determined by the comparison of measured and simulated gap fractions. We simulated gap fractions at the 185 DCP measured locations by FLiES, changing leaf and woody area densities and fitting the simulated gap fractions to the measurements. Using this comparison approach, we found the minimum root mean square (RMS) difference between the measured and the simulated gap fractions (Figure 4). The leaf area density (LAD) and woody area density (WAD) were 0.52 ± 0.11 and 0.56 ± 0.14, respectively. LAI computed from this LAD was 1.02 around the litter fall trap area (No 3. in Figure 3). The independent LAI measurement by the litter fall trap was 1.27 ± 0.41 (95% confidence interval); the DCP-derived LAD was within the error of the litter fall trap. When we applied this LAD to areas No. 1, No. 2, and No3, the average landscape LAIs were 0.59, 0.57, and 0.51, respectively.

The spectral reflectance of the soil and stems were measured with a field spectrometer (MS-720, Eko Instruments, Japan) with 25 degrees field of view. The spectral range of the MS-720 was 350 nm - 1100 nm with a spectral resolution of 10 nm. The soil reflectance (Table 2) is an average of several different ground conditions including bare soils, and the ground covered by some dead leaves. Reflectance and transmittance of oak and grass leaves were measured at the laboratory. We used a spectrometer (USB2000, Ocean Optics) with an integrating sphere (LI-1800-12S, LI-COR Inc., Lincoln, NE, USA). We assumed that the reflectance and transmittance were the same for all the leaves (see Table 2).

3.2.3 Canopy reflectance – AVIRIS data-

Airborne Visible/Infrared Imaging Spectroradiometer (AVIRIS) data were used to evaluate the simulated canopy reflectance (nadir view spectral bidirectional reflectance) at landscape scale (No. 1 in Figure 3). We used AVIRIS images collected on May 12, 2006 and on August 5, 2007. Both AVIRIS images were obtained under clear sky conditions. The spatial resolutions of these data were 3.2 m - 3.4 m, depending on the flight altitudes. The two images were spatially matched and geo-rectified using ground control points; RMS errors were less than one pixel (i.e. ~3 m). Atmospheric corrections were applied to the two AVIRIS images in order to obtain the nadir view spectral reflectance at the surface. We used ACORN software (ImSpec LLC, Analytical Imaging and Geophysics LLC, Boulder, CO, USA) for atmospheric correction. We simulated the spectral bidirectional reflectance at three visible wavebands, and at two NIR wavebands. The bandwidth of each band was 10 nm centered at 450 nm, 550 nm, 650 nm, 780 nm, and 900 nm.

3.2.4 Understory radiation measurements

We used a 20 m-long traversing radiometer system (No. 3 in Figure 3) for downward and upward PAR and net radiation measurements. This radiometer system is equipped with sensors that measure PAR (PAR-LITE, Kipp & Zonen, Netherlands), and net radiation (NR-LITE-L, Kipp & Zonen, Netherlands) at 1 m above the ground. This system moves back and forth along a rail track. It takes about 12 minutes to complete a one-way measurement. The western half of the rail track is under the oak trees, and the eastern half is in open space. Radiation flux densities were measured every second (~0.027m intervals) and we averaged data over every 1 m interval. We selected four days for the comparisons (Table 1), which included different meteorological and ground conditions: one comparison with a day of fully foliated trees over green grass (DOY 124) and three comparisons with days of fully foliated trees over dead grass (DOY 130, 194, and 215).

We measured spectral transmittances in the understory along the two transects (Transects A and C in Figure 3) at 1 m intervals. We used a spectrometer, as described in 3.2.1 (MS-720, Eko Instruments, Japan). For spectral transmission measurements, we

used hemispherical field of view. The times of the measurements were from 10:18 am to 10:24 am for Transect A and from 10:59 am to 11:05 am for Transect C. It was mostly sunny during the observation times. Before and after the measurements, we took one spectral radiation measurement over a large open space as a control. Spectral transmittances were calculated as a ratio of radiations along transects and open space radiations. We extracted three visible wavelengths (450 nm, 550 nm, 650 nm), and two NIR wavelengths (780 nm, 900 nm) where the width of the wavelength was 10 nm.

3.2.5 Flux tower measurements

Eddy covariance and meteorological variables were measured at the top of the tower, which is located at the center of area No. 2 (Figure 3). The height of the tower is 23 m, where downward and upward PAR, net radiation, and energy fluxes were measured. Details of the experimental design are summarized in Baldocchi et al. (2004) and Ma et al. (2007). We used meteorological measurements as inputs, including air temperature, solar radiation, PAR, air pressure, CO_2 concentration, wind speed, and water vapor pressure. For diffuse PAR and incoming TIR, we used measurements from a nearby tower at the Vaira Ranch site (38.418 N, 120.958 W), about 2 km away from our study site. Before DOY 193, 2008, there were several missing periods for the incoming TIR data. For these periods, we estimated incoming TIR with the Brutsaert model (1975).

We chose four periods of seven consecutive days to test the 3D model (Table 1). These periods included leafless trees with green grass understory (DOY 68-74), fully foliated trees with green grass understory (DOY 115-121), and fully foliated trees with dead grass understory (DOY 188-194 and DOY 204-210). To compare the PAR albedo, net radiation, sensible heat flux, and latent heat flux, we averaged the measurements over seven days. Averaging of eddy flux data over several days was necessary to minimize the influence of the stochastic nature of turbulence and the spatial variability of the trees (Baldocchi and Wilson, 2001). For the test of the simulated oak canopy photosynthesis, we used tree gross primary productivity (GPP) data sets, which were calculated by subtracting the total ecosystem GPP estimated by the CO_2 flux at overstory tower from the understory GPP estimated by the CO_2 flux at the understory

436 tower located in area No. 3 (Ma et al., 2007).
437
438 ## 4. Results and discussion
439
440 ### 4.1 Canopy reflectance
441
442 Comparing the simulated canopy reflectance with AVIRIS data, the simulated
443 red, green, and blue composite images generally well-represented the spatial patterns of
444 the tree crowns and the woodland understory (Figure 5). Pixel by pixel comparisons
445 show that the RMS errors and biases on May 12, 2006 were 0.018 and 0.0058 for
446 visible channels, and 0.12 and 0.096 for NIR channels, while the RMS errors and biases
447 on August 5, 2007 were 0.029 and -0.016 for visible channels, and 0.063 and 0.0014 for
448 NIR channels.
449
450 For May 12, 2006, the simulated canopy reflectance by the 3D scheme in the
451 NIR domain (780 nm and 900 nm) were 34% - 39% larger than the AVIRIS
452 reflectance (Figure 6a). The reflectance contributions from the crown, woody elements,
453 and the surface were 12%, 10%, and 78% at 650 nm and 30%, 3%, and 67% at 780 nm.
454 Since most of the large open spaces were exposed bare soil (Figure 5), we conducted an
455 additional 3D simulation using the bare soil reflectance data without the grass layer. The
456 spectral pattern assuming bare soil was closer to the AVIRIS data than when using the
457 grass layer. The RMS errors and biases were 0.020 and 0.0097 for visible channels, and
458 0.073 and -0.015 for NIR channels. The reflectance contributions from the crowns, the
459 woody materials, and the surface were then 9%, 7%, and 84% at 650 nm, and 43%, 4%,
460 and 53% at 780 nm, respectively. Because of the low crown cover (47%), reflected
461 radiance from the surface layer contributed substantially to canopy reflectance
462 (53%-84%). Under such conditions, the difference between grass LAI measurements
463 and actual spatial variations in grass differentiated the canopy reflectance, as most of
464 the large open spaces were exposed soil or dead leaves. Indeed, our ground-based
465 measurements (the data are not shown here) of spectral reflectance show that NIR
466 reflectance of the open space near our study site was 0.05 (reflectance unit) higher than
467 that of under the tree crowns in the similar period (May 11, 2007).
468

The simulated canopy reflectance by the 3D scheme for August 5, 2007 (when green grass was absent) show a similar spectral pattern to the AVIRIS one (Figure 6b). The reflectance contributions from the crowns, woody materials, and the surface were 6%, 5%, and 89% at 650 nm and 36%, 4%, and 60% at 780 nm. For the August 5, 2007 results, we also evaluated average canopy reflectance of the crowns and the soil surface separately (Figure 7). We separated the crown areas from the soil by applying a single threshold to AVIRIS and simulated 650 nm (red) images. Using thresholds of 0.13 (AVIRIS) and 0.1 (simulated), the crown areas were separated from the soil surface. Spectral patterns for the AVIRIS and simulated canopy reflectances were similar for both crowns and the soil surface (Figure 7). The differences between the AVIRIS and the simulated canopy reflectances by the 3D scheme were less than 0.03 in reflectance unit in most cases, indicating that the reflectance of each components agreed fairy well.

Although some previous studies pointed out the noticeable influence of woody elements on canopy reflectance (Malenovsky et al., 2008; Verrelst et al., 2010), the reflected contribution from the woody elements was marginal and the contributions from the soil surface were dominant. In the red (650 nm), the reflected contribution of woody elements was comparable to that of the oak leaves. This was the case because the reflectance of woody elements in 650 nm (0.218) is much higher than that of oak leaves (0.075) (Table 2). Therefore, the contributions of woody reflectance tended to be higher, but since the oak leaves were distributed in the outer domains (Figure1), these leaves likely moderated the reflectivity effect of woody elements. Photons are likely to first hit oak leaves rather than branches and stems (Kucharik et al., 1998). In NIR, reflectance and transmittance of the oak leaves were much higher than those at 650 nm (Table 2) and the reflectance contributions from woody elements were much lower than those of the oak leaves.

Figure 6 also shows the spectral canopy reflectance simulated by the 1D scheme with the same tree canopy LAI (=0.59) and WAI (=0.36) as we ran the 3D scheme. The spectral canopy reflectance by the 1D scheme was close to those of the 3D model. This is because the canopy spectral reflectance was greatly affected by the understory conditions at our study site. As described above, the radiance contribution from the ground surface was from 84 to 89 % in red (680 nm) and from 53 to 60 % in

NIR (780 nm). Given the sun and view zenith angles and low LAI conditions, the canopy architecture was not a primary factor for the canopy reflectance in our study condition, although the importance of the canopy architecture to canopy reflectance depends on the view geometry and LAI (e.g. Widlowski et al, 2007).

4.2 Radiation budget at the understory level

Characterizing the understory radiation budget is of particular importance for heterogeneous landscapes because of their high proportion of net radiation (available energy); the absorbed radiations are redistributed as sensible, latent and soil heat fluxes. The evaluation of the spatial pattern of the understory was also important for the sampling design of energy fluxes and the footprint analysis of energy balance measurements. Spectral dependency of transmittances revealed a scattering effect on the transmitted radiation (Figure 8). In the NIR, the tree leaves were highly reflective and transmissive so that multiple scatterings among these elements enhanced light transmittance of the tree canopy. The results from two transect with the 3D scheme show that transmittances in the NIR were 0.05-0.07 (9%-11%) higher than those in visible domain. The simulated results by the 3D scheme from the two transects (A and C) agreed reasonably well with the measured transmittances; the biases were 0.013 for Transect A and 0.024 for Transect C. When we did not include the woody elements, transmittances were 0.2-0.25 higher than those of the measurements. In addition, the slopes of regression lines were much steeper than the 1 to 1 line (slope = 1.47). This indicates that the woody elements suppressed the multiple scattering, as they blocked the solar radiation. The spectral transmittances simulated by the 1D scheme with the average LAI (=1.12) and WAI (=0.68) around the two transects were lower than those of the 3D model. When the woody area was not considered, the transmittance in the visible spectral domain was as low as 0.4. The slopes of these two 1D cases (with woody and without woody) were much steeper than those of the 3D cases. The comparisons of the 3D and 1D schemes and the woody and non-woody conditions indicate that consideration of both 3D canopy architecture and woody elements is required to model the canopy transmission, and thus the available solar radiation at understory vegetation.

535 Figure 9 shows downward and upward PAR, and net radiation along the
536 traversing radiometer system (Figure 3) in the morning (10:00 pm), noon (12:00 pm),
537 and afternoon (15:00 pm). Since the eastern half of the rail track was across an open
538 space (Figure 3), it was exposed to full sunlight until noontime— downward PAR and
539 net radiation on this side were almost constant. The western half of the rail track was
540 located under the tree canopy. Therefore, the transect variability of downward PAR was
541 associated with the sunlit and shaded areas that were formed as a geometric relationship
542 between the tree crowns and the sun direction. Until noon, the model captured the
543 radiation variability along the rail track. However, in the afternoon, our model did not
544 capture the variability along the rail track. Although upward PAR was low due to the
545 low ground reflectance in the PAR region (Table 2), the variability in upward PAR
546 along the rail track was similar to those of downward PAR (Figures 10).
547
548 Figure 10 shows diurnal patterns of simulated and measured downward and
549 upward PAR, and R_n. The data shown here are averaged values along the rail track.
550 Table 3 shows statistics of the comparison between simulated and measured radiation
551 values. The simulated results capture the general diurnal patterns of downward and
552 upward PAR and R_n. There are two reasons for the differences between the measured
553 and simulated radiation. First, the differences in crown sizes and positions between
554 modeled and actual trees around the rail track resulted in different downward and
555 upward flux densities of PAR and R_n. For example on DOY 194 15:00 pm (Figure 9c),
556 the peaks of the simulated PAR and R_n were found at about 10 m on the rail track. These
557 peaks should have been aligned with the measured peaks at 12 m. In the afternoon, the
558 sunlight comes from the west, where the track is shaded (Figure 3), and the crowns cast
559 elongated shadows eastward. Therefore, the spatial variation in downward PAR and R_n
560 along the rail track were formed by smaller scale gaps between and inside the crowns,
561 which are more sensitive to the individual crown shapes and lengths. The assumption of
562 the spheroid crown shape with turbid volumes blurred when simulating the small-scale
563 variability of the solar radiation at the understory. The second reason for the differences
564 is the spatial variation in LAD and WAD in the crown object. Our model assumed that
565 LAD and WAD were constant in the crown volumes. However, because of the actual
566 spatial variability of LAD and WAD in the crowns, gap fractions did not match exactly.
567 For example, the simulated LAD, which can fit well with the measurements, depends on

568 the position of the transects (Figure 4). For the simplicity of the modeled trees, we
569 assumed that there was a constant LAD and WAD inside the crown objects. That could
570 cause differences of PAR and R_n at the understory level.
571
572 Transect-based measurements along the rail track have an advantage in that
573 they produce spatially representative radiation environments. In particular,
574 measurements from transects placed perpendicular to the sun direction maximize the
575 spatial representation (Widlowski, 2010). Our rail track was placed along the east-west
576 direction; it gave the maximum variety of radiation spatially as the beam lights came
577 from a southerly direction around noontime. There was, however, a limitation on the
578 length of the rail track (20 m). For example, to evaluate the radiation environment over
579 the coverage of the eddy covariance footprint, we needed to deploy at least more than a
580 100 m transect. Such long transect measurements require faster velocity of the tram to
581 keep the suite of track measurements in a same solar geometry, but they reduce the
582 frequency of spatial samplings for the net radiometer as net radiometers have slower
583 response (~30 second) to the subtle changes in radiation environments.
584
585 **4.3 Energy flux densities and canopy photosynthesis**
586
587 Figure 11, 12 and Table 4 show the comparisons between the simulated (both
588 3D and 1D schemes) and measured energy flux densities (R_n, H, λE, and G) in four
589 different periods. In the 1D scheme, we did not include the woody elements because
590 most of the 1D land surface models do not consider the sensible heat and heat storage of
591 the woody elements. The comparison covers three distinct seasons, (1) leafless crowns
592 with green grass (DOY 68-74), (2) fully foliated crowns and green grass (DOY
593 115-121) and (3) fully foliated crowns and dead grass with water deficits (DOY
594 188-194, 204-210). The simulated and measured R_n generally exhibited the similar
595 seasonal and diurnal patterns. However, the peak R_n simulated by the 3D model was 4
596 to 11 % higher than the measurements, while the peak R_n by the 1D model agreed well
597 except the DOY 68-74 (8 % error). The RMS errors show that H, λE, and G simulated
598 by the 3D scheme were better than those of the 1D scheme (Figure 12). In the 1D
599 scheme, the large differences were found in DOY 68-74 and DOY 115-121 when the
600 weather is mild and the soil is wetter (Table 1); Sensible heat flux densities simulated by

601 the 1D scheme tend to be lower in those periods, and latent heat flux densities tend to be
602 higher than the measurements. In the 1D scheme, the understory grass and the soil
603 surface received more radiation than those of the 3D scheme because of the lack of the
604 woody elements over the understory. For example, in DOY 68-74, the fraction of
605 absorbed PAR (FAPAR) simulated by the 1D scheme was 24 – 42 % higher than that of
606 the 3D scheme. This caused an overestimation of absorbed radiation in understory grass
607 and soil. Consequently, this effect led to overestimation of the latent heat fluxes of grass
608 and soil. In DOY 115-121, tree leaves and understory grass co-existed. In this period,
609 FAPAR of the 1D scheme is higher than that of the 3D scheme, and this caused
610 overestimation of latent heat flux.
611
612 On the contrary, the differences between 3D and 1D schemes in the dry
613 periods (DOY 188-194 and 204-210) were smaller. The simulated results from both
614 schemes agreed fairly well with the measurements even though FAPAR from both
615 scheme had some differences (Figure 13). In such periods, due to limited soil water
616 availability, the soil evaporation was negligibly small and the trees closed most of their
617 stomata, inhibiting the transpiration. As a result, most of the absorbed energy was used
618 as sensible heat.
619
620 The simulated energy fluxes by the 3D scheme closed $(H + \lambda E) / (Rn - G - S_{woody}) = 1$. If we exclude the woody storage components, the simulated daytime and
622 nighttime energy balance closure $(H + \lambda E) / (Rn - G)$ were 0.88 and 0.77, respectively.
623 On the other hand, the daytime and nighttime energy balance closure of the eddy
624 covariance measurements $(H + \lambda E) / (Rn - G)$ were 0.81 and 0.17, respectively. For the
625 daytime case, the simulated results show the woody storage term accounts for 0.12
626 (12%) of all energy fluxes. The consideration of the landscape scale woody storage term
627 significantly improves the accuracy of the measured energy balance closure (from 0.81
628 to 0.93). For nighttime case, due to low wind and larger flux footprint, the energy
629 balance closure was significantly lower than 1. The consideration of the woody storage
630 term potentially improve the energy balance closure, however, the large uncertainty of
631 the measurements impedes evaluating evaluation the role of the nighttime stem storage
632 flux. Energy imbalance has been one of the important issues and therefore has been
633 investigated thoroughly (Wilson et al., 2002). For example, Lindroth et al. (2010) found

634 the significance of including the woody storage component in spruce/pine forests. Our
635 study site also shows a substantial contribution of woody storage due to a
636 heterogeneous landscape and high proportion of woody area to total plant area.
637
638 Figure 14 shows the diurnal patterns of the simulated (3D and 1D) and the
639 measured tree canopy photosynthesis (P_s) (Ma et al., 2007). For DOY 115-121, with the
640 moderate air temperatures (10°C-24°C) and sufficient soil water available to the trees
641 (Table 1), P_s was the largest among the three compared periods. The P_s simulated by the
642 1D scheme was large than the 3D scheme in the morning. This is because the FAPAR of
643 the 1D scheme is higher than the 3D scheme (Figure 14). Moreover, VPD and air
644 temperature are milder in the morning and less stress than the afternoon (Figure 14).
645 Thus, the P_s in the morning is more sensitive to the difference in FAPAR than that in the
646 afternoon. On DOY 188-194 and 204-210, due to the high temperature and VPD, P_s was
647 strongly down-regulated by these factors as well as by a low V_{cmax} (Ma et al., 2011). The
648 differences between the 3D and 1D scheme were small in those periods. Overall, the 3D
649 scheme (RMSE=1.15) performed slight better than that of the 1D scheme (RMSE=1.56)
650 (Figure 15).
651
652 **4.4 Spatial variations of radiation fluxes across the canopy heights**
653
654 Since our study site is heterogeneous a mismatch of the simulated and
655 measured radiation fluxes in Figure 11 was likely. We analyzed how the heterogeneity
656 of the landscape affected the spatial variation of the radiation fluxes around the flux
657 tower location in area No. 2. Figure 16 shows upward PAR, NIR, TIR, and R_n at three
658 different heights (understory level = 1 m, just above the canopy = 12 m, and the flux
659 tower height = 23 m). As the sampling height increased, spatial variations of radiation
660 fluxes were rapidly reduced. The standard deviations of the radiation fluxes at the flux
661 tower height (23 m) were 1.3-16.4 W m^{-2} and their coefficients of variations were 6.8%
662 for upward PAR, 4.2% for upward NIR, 2.8% for upward TIR, and 2.1% for R_n.
663 Therefore, the spatial variations in the radiation streams were small. The reason why the
664 spatial variations were small is attributed to the angular contributions of the incoming
665 radiation of the PAR and R_n sensors. The contribution of incoming radiation to the PAR
666 and R_n sensors is proportional to $\cos\theta_o$ integrated over the sphere (or hemisphere) with a

667 weight of $\sin\theta_o$ (Jacobian), where θ_o is a view zenith angle. Based on this weight , only
668 12% of radiation energies could be attributed to field of view < 20 degrees, which is
669 about the radius of 8.4 m at the ground. While we found a similar size of open space
670 just below the flux tower location, that open space did not significantly affect the
671 representativeness in measuring the landscape scale radiation fluxes.
672
673 **4.5 Effect of woody elements on radiation absorption by canopy**
674
675 In CANOAK-FLiES, we explicitly defined woody areas in the crowns. We
676 estimated the woody area density from the gap fraction measurements based on digital
677 cover photography. Moreover, our energy flux simulation implies a significant amount
678 of the woody heat storage. Figure 13 shows diurnal patterns of a fraction of the
679 absorbed PAR (FAPAR) and a fraction of the absorbed NIR (FANIR) in four simulated
680 periods. These results exhibited general temporal patterns found in previous research
681 (Widlowski, 2010). Generally, absorptions by woody elements were lower than those
682 of leaves, but they were not negligible. The FAPAR and FANIR of the woody elements
683 contributed 12%-39% and 20%-52% of the total FAPAR and FANIR, respectively
684 (Figure 13). Particularly, in the NIR domain, leaf transmittance was higher than that in
685 the PAR domain (Table 2), resulting in the higher absorption in woody elements via a
686 contribution of radiation transmitted through the leaves. Due to the nature of the
687 woodland structure at our site, the higher proportion of woody area to leaf area (42%)
688 (Ryu et al., 2010a), caused a higher absorption in woody elements. Our results support
689 the radiative transfer study by Asner et al. (1998), which also shows a large amount of
690 PAR absorption in woody elements (10-40%).
691
692 **4.6 Overall performance and uncertainties of the 3D approach**
693
694 The spatially explicit 3D radiative transfer and energy exchange model,
695 CANOAK-FLiES, was developed to simulate spatial distribution of radiation
696 environments and energy and carbon fluxes. Recent advancement in obtaining detail
697 canopy structure and radiation data sets enabled us to develop and validate this type of
698 3D model. We employed airborne-based LiDAR data proposed and validated by Chen
699 et al. (2006). While CANOAK-FLiES mostly captured the spatial and temporal patterns

of radiation environments, the current airborne-LiDAR data has a limitation in extracting a canopy structure finer than a 1-2 m scale. In that scale, the use of ground-based LiDAR data improves the description of radiation environments (Hosoi and Omasa, 2007; Zande et al., 2009). Our 3D approach relies on the accurate canopy structural parameters derived from the airborne LiDAR data. Currently, the availability and uncertainty of such data limit extending the 3D approach to other ecosystems. For example, Disney et al. (2010) investigated the expected accuracy of the canopy height retrieval from the discrete-return LiDAR system and found that the LiDAR based approach tended to underestimate the canopy height. Hoskinson (2007) also showed that the canopy heights retrieved by the LiDAR was sensitive to the sampling strategy such as flying altitude, laser pulse repetition frequency. The errors in the crown heights and diameters could change the landscape heterogeneity. Underestimation of such parameters causes smaller crown volumes and thus overestimation of leaf and woody area densities as we estimate these variables by matching the simulated gap fraction constructed by the 3D canopy with the gap fractions taken by the digital photography. Consequently, underestimation of the canopy structural parameters can cause severe clumping, and lower tree FAPAR, λE, and P_s. In other words, the improvement of canopy structure observation makes the model performance better. Nonetheless, the 3D approach will be useful to fill the theoretical gap between 1D model and the real ecosystems. Therefore, the improvement of the LiDAR algorithms will be important.

In most of the past studies, 3D models were evaluated by transect variability or diurnal patterns of PAR transmittance measurements (Law et al., 2001; Sinoquet et al., 2001; Tournebize and Sinoquet, 1995; Wang and Jarvis, 1990), but few modeling studies have tested the spatial variations of net radiation in heterogeneous landscapes. In this study, we evaluated not only PAR transmittance, but also NIR, and the net radiation at the understory and at the top of the canopy. Reliable simulation of net radiation is needed when computing energy fluxes. Therefore, reliable radiative transfer simulation in the TIR domain is crucial, and the TIR radiation can be simulated from leaf temperature variations that are computed by the energy exchange model. We completed the simulation by coupling the radiative transfer model with the energy exchange model. Also, spectral reflectance (bidirectional reflectance) and spectral transmittance allowed us to evaluate the effect of scattering on transmittance and reflectance. Since our 3D

733 model results of canopy reflectance and transmittance agreed well, the absorption (=1 –
734 reflectance – transmittance) simulated by the 3D model should be reliable. Furthermore,
735 we also simulated radiation fluxes at several different vertical levels, including the
736 understory and the top of the canopy. Even though the tower was located in an open
737 space, contribution of the radiation flux from the understory level was marginal, as the
738 spatial radiation fluxes blurred with an increase in the height.
739
740 The CANOAK-FLiES simulation in 3D and 1D modes enabled us to examine
741 the effect of landscape heterogeneity on energy and carbon fluxes through the change in
742 the simulated canopy radiation environments. Overall, the 3D scheme worked better
743 than the 1D scheme. The effect of landscape heterogeneity depends on the radiative
744 quantities. The difference between 3D and 1D schemes was negligible in canopy
745 reflectance, but substantial in canopy absorption (FAPAR) and transmittance. The
746 impact of heterogeneity on these radiation quantities will also depend on the stand
747 structure such as canopy LAI and crown cover. Wherever such diverse landscape
748 conditions, the 3D approach is expected to provide better solutions. This fact
749 encourages re-designing the model-data intercomparison study based on the different
750 level of model complexities from 3D (close to the actual ecosystems) to 1D with a finer
751 time scale (hourly). While the existing intercomparison studies are likely to extract
752 where to give wrong water and carbon fluxes via statistical or tuning approaches (e.g.
753 Ichii et al., 2010; Mahecha et al., 2010, Morales et al., 2005; Schwalm et al., 2010), a
754 hierarchical model comparison approach with process-based understanding would
755 improve the model reliability avoiding flaws of physics and physiology.
756
757 Regarding λE and P_s, the 3D scheme generally performed better than the 1D
758 scheme. Yet, our comparison study reveals that the importance of accounting for the 3D
759 canopy structure changes with other meteorological and physiological conditions. The
760 notable λE and P_s differences were found in wet mild weather periods (Figure 11 and
761 14) because relative contribution of radiation environment to those fluxes were
762 dominant in such periods. These results partly agree with the study by Song et al.,
763 (2009) as they concluded that the heterogeneous canopy yielded lower λE and P_s at the
764 loblolly pine stand. In the dry periods, however, the λE and P_s differences between 3D
765 and 1D scheme were not clear. According to the analysis by Chen et al., (2008), the

differences of the canopy architecture modeled under the dry seasons with low LAI did not give a substantial difference in P_s simulation. Our results, the difference of the canopy architectures (3D or 1D) were not relevant to P_s in dry season, also coincided their results since the P_s is mostly controlled by the water availability via a change in photosynthetic capacity (V_{cmax}). These results indicate that the light-limited (wet mild weather) periods force more reliable treatment in radiative transfer simulation than the water-limited periods (dry hot weather). Further study is necessary to investigate how the difference of the canopy structural modeling affects the seasonal and interannual variations in energy and carbon fluxes. In that situation, the intermediate complexity approach could fill the gap between 3D and 1D approach. For example, Chen et al. (2008) constructed oak woodland landscapes by box-shaped trees and used to simulate canopy photosynthesis. While P_s difference among the models with different complexity was negligible in dry periods, their intermediate complexity approach should also be tested in wet mild periods because our results suggest that the effect of canopy structure on canopy photosynthesis is large in wet mild periods. Applying this intermediate complexity approach to the wed mild periods, combined with our 3D approach, will provide how well and efficiently the models simulate the water and carbon fluxes.

This study indicates that the appropriate consideration of woody elements in the heterogeneous landscape is crucial for partitioning the radiation environments (transmittance, absorption, and reflectance). The absence of woody elements resulted in higher transmittances (Figure 8). In the NIR domain, woody elements inhibited the enhancement of the scattering radiation to some extent. The absorption of woody elements was also significant (12%-39% in PAR and 20%-52% in NIR). Consequently, the effect of woody elements on the energy balance simulation was not negligible. Indeed, our simulated results suggest that 12% of available energy should be used for heat storage in woody elements. On the other hand, the effect of woody elements on the canopy reflectance was marginal because the crown cover was low (47%) and many photons that first hit the leaves were scattered. Given that the high portion of the woody area, the accurate estimate of the woody area density leads to the robustness of the estimates of the radiation environment and the energy fluxes including the heat storage term. We estimated woody area density by matching the simulated and measured gap

799 fractions. However our best estimate of woody area density lies on 25% error. In
800 addition, the crown architecture we assumed is still simpler than reality; there is no
801 interdependence between the location of leaves and branches. In fact, leaves are clumped
802 around the woody elements like twigs and formed as a shoot. Our crown assumption may
803 lead overestimate or underestimate to the woody light absorption. The improvement of
804 the airborne and ground LiDAR-based canopy architectural estimate and more realistic
805 tree modeling will reduce these uncertainties.
806
807 Further studies are needed to add modules that have not been included in our
808 model. Soil water effects on photosynthesis and evaporation were prescribed; we used
809 soil moisture and photosynthetic capacity (V_{cmax}) measurements for computation of soil
810 evaporation and photosynthesis. Radiative transfer processes were fully modeled in 3D
811 space explicitly, but the turbulence scheme was still one dimensional and assumed the
812 concentration field was well mixed in the horizontal. This assumption could cause an
813 error for the concentration field within the crown objects. However, in our study site,
814 this effect should not cause a major source of the error in simulating energy fluxes since,
815 in our model, leaves are distributed on the outer side of the crown canopies (Figure 1),
816 where the concentration field are in between the open space and the inside crown. We
817 assumed that the crowns were spheroid with the same leaf area density. We divided the
818 radiation into three broad spectral bands (PAR, NIR, TIR). Exploring the optimized
819 number of spectral bands improves the radiative properties. One of the advantages of
820 the Monte Carlo radiative transfer model is that the computation time does not increase
821 when we divide the spectral domain into more than three spectral domains; the
822 statistical accuracy of radiation only depends on the total number of photons.
823 Nonetheless, improvement of the computation time is necessary when the model is run
824 over a yearly time scale. In this study, diffuse sky radiances were assumed to be
825 isotropic. Realistic information of angular variations in atmospheric diffuse radiation
826 improves the accuracy of energy fluxes and photosynthesis (Hutchison et al., 1980).
827
828

5. Conclusion

We coupled a 3D shortwave and longwave radiative transfer model with an energy and carbon exchange model (CANOAK-FLiES). This type of detailed modeling and testing was achieved by collecting spatial and temporal shortwave and longwave radiation data sets as well as other plant physiology and energy flux data sets. In particular, the tree structural information from airborne-LiDAR enabled us to make a direct comparison of the spatial radiation environments with measurements. We evaluated the simulated radiation fields in several different spectral domains (PAR, NIR, net radiation, and finer spectral domains of AVIRIS spectra) including spatial and temporal patterns at understory and top of the canopy levels. Accurate computation of the radiation environments assures the reliability of the computation of energy fluxes.

Our model mostly captured the spatial and temporal patterns of radiation environments larger than a 1-2 m spatial scale. At the understory level, our model was able to simulate the spatial and temporal patterns in PAR and net radiation, including the distinct patterns between the open and shaded areas. At the top of the flux tower, in spite of a heterogeneous condition at our study site, the spatial variability of the net radiation was small. Vertical profiles of radiation fluxes suggest that the spatial heterogeneity of radiation field blurred rapidly as the sensor height increases.

The comparison between 3D and 1D schemes revealed that the 3D scheme generally performed better than the 1D scheme. However, the importance of accounting for the 3D canopy structure changes with other meteorological and physiological conditions. The 3D approach is more important in wet mild (light-limited) periods than dry (water-limited) periods. The significant λE and P_s differences were found in wet mild weather periods because of high radiation sensitivity to λE and P_s.

When LAI is low and the fraction of woody elements is high like our study site, explicit consideration of the woody elements (branches and stems) is crucial for realistic computation of radiation environments and energy fluxes. The significance of woody elements depends on the radiative properties (canopy reflectances, FAPAR, spectral transmitted light at the understory level). A significant amount of radiation was

862 absorbed in the woody elements and used for heat storage. Consideration of woody
863 elements improved the daytime energy balance closure and afforded an accurate
864 partitioning of energy fluxes.
865
866 Since CANOAK-FLiES has a spatially explicit 3D structure, the model is
867 useful for the spatial analysis of radiation environments and energy fluxes. The model
868 can help us to understand the observations of heterogeneous landscapes and to check the
869 spatial representativeness and design of measurements. Improvements in computational
870 efficiency, especially for radiative transfer schemes, are necessary to run the model over
871 a yearly time scale and larger spatial scale.
872

Appendix A Nomenclature

A: Surface area of a simulated landscape (m^2)

$E_{tir,tot}$: Total thermal emission in a simulated landscape (W)

$E_{tir,s}$: Thermal incoming radiation from the sky (W)

$E_{tir,c}$: Thermal emission from trees (W)

$E_{tir,g}$: Thermal emission from ground (W)

λE: Latent heat flux (W m^{-2})

G: Soil heat flux (W m^{-2})

H: Sensible heat flux (W m^{-2})

I_{tir}: Thermal incoming radiation from the sky (W m^{-2})

P_E: Thermal emission probability distribution function

R_{abs}: Absorbed shortwave (PAR and NIR) plus incoming longwave radiation (W m^{-2})

R_{PAR}: Absorbed PAR (W m^{-2})

$R_{PAR,beam}$: Absorbed beam PAR (W m^{-2})

$R_{PAR,diffuse}$: Absorbed diffuse PAR (W m^{-2})

R_{NIR}: Absorbed NIR (W m^{-2})

R_{TIR}: Absorbed TIR (W m^{-2})

S_{woody}: Heat storage in woody elements (W m^{-2})

T_l: Leaf temperature (C)

T_w: Woody temperature (C)

T_g: Soil temperature (C)

g_L: Leaf angle distribution

u: Leaf area density (m^2 m^{-3})

w: Woody area density (m^2 m^{-3})

$\Omega_s(\theta_s,\varphi_s)$: Sun direction vector

$\Omega_l(\theta_l,\varphi_l)$: Leaf surface normal vector

$\Omega_E(\theta_E,\varphi_E)$: Direction vector of thermal emission

α, α_θ, α_φ: Random number

ε_g: Emissivity of the soil surface

ε_l: Emissivity of leaves

ε_w: Emissivity of woody elements

σ: Stephan-Boltzmann constant (= 5.67 x 10^{-8}) (W m^{-2} K^{-4})

906

Appendix B Determination of the position of photon emission and the direction of photon emission

The total emission energy of a landscape can be written by:

$$E_{tir,tot} = E_{tir,s} + E_{tir,c} + E_{tir,g}, \quad \text{(B-1)}$$

where E_{tir} (W) is an emission energy, and the subscripts of *tot*, *s*, *c*, *g* indicate the emission energies of the total, the sky, the trees (the leaves plus the woody elements), and the ground emission energies. $E_{tir,s,}$ was calculated by:

$$E_{tir,s} = I_{tir} A, \quad \text{(B-2)}$$

where I_{tir} (Wm^{-2}) and A (m^2) are incoming TIR energy and a horizontal area of the landscape, respectively. I_{tir} was obtained either from observations or simulations of atmospheric radiative transfer model. Similarly, the emission from the ground, $E_{tir,g,}$ was derived by integrating the local emission (= $\sigma\varepsilon_g T^4_g(\mathbf{r})$) over the ground surface (S):

$$E_{tir,g} = \sigma\varepsilon_g \int_s T_g^4(\mathbf{r}) dS, \quad \text{(B-3)}$$

where σ (W m^{-2} K^{-4}) is the Stephan-Boltzmann constant (= 5.67 x 10^{-8}). ε_g is an emissivity of the ground. We assumed a constant emissivity of the ground (ε_g=0.98) over the simulated landscape. On the ground, the surface temperature varies with location due to the difference in the radiation conditions; some areas are exposed to sunlight and others are shaded. Total emission from the ground was, therefore, calculated by integrating the emission at each point ($\mathbf{r}$) over the landscape. Regarding the emission from trees, $E_{tir,t}$, the contribution from both leaf and woody surfaces was considered. E_t was derived by integrating the local emission (=$\sigma\varepsilon_l T^4_l(\mathbf{r})u(\mathbf{r})$+ $\sigma\varepsilon_w T^4_w(\mathbf{r})w(\mathbf{r})$):

939 $$E_{tir,t} = 2\sigma \int_v \left\{ \varepsilon_l T_l^4(\mathbf{r}) u(\mathbf{r}) + \varepsilon_w T_w^4(\mathbf{r}) w(\mathbf{r}) \right\} dV \quad , \qquad \text{(B-4)}$$

940

941 where ε_l and ε_w are emissivity of leaf and woody materials. We multiplied by 2 to
942 obtain the total emission from the both adaxial and abaxial sides, as u and w are
943 defined by one side of the leaf and one side of the woody surface areas. Finally, the
944 probability distribution function, $P_E(\mathbf{r})$, was obtained by:

945

946 $$P_E(\mathbf{r}) = \frac{E_{tir}(\mathbf{r})}{E_{tir,tot}} \quad , \qquad \text{(B-5)}$$

947

948 where $E_{tir}(\mathbf{r})$ is a local emission in the simulated landscape,

949

950 The spatial distribution of photon emission needed to follow $P_E(\mathbf{r})$. We
951 determined emission positions by two steps. First, we determined an emission
952 category such as emission from the sky, trees, or ground, and then we determined an
953 emission position.
954 The emission category was determined by a uniform random number, α=[0,1),
955 and the following criteria:

956

957 $$0 < \alpha < \int_{sky} P_E(\mathbf{r}) dS$$

958 for sky (B-6a)

959 $$\int_{sky} P_E(\mathbf{r}) dS < \alpha < \int_{sky} P_E(\mathbf{r}) dS + \int_{trees} P_E(\mathbf{r}) dV$$

960 for trees and understory grasses (B-6b)

961 $$\int_{sky} P_E(\mathbf{r}) dS + \int_{trees} P_E(\mathbf{r}) dV < \alpha < 1$$

962 for ground (B-6c)

963

964 Once the emission category was determined, a possible candidate of the emission
965 position, $\mathbf{r}=(x, y, z)$, in the selected category was determined using random numbers. To
966 obtain the emission position that followed an emission energy distribution, we used a

rejection technique (Press, 1992). The criterion to select the position was:

$$\alpha < \frac{E_{tir,i}(\mathbf{r})}{E_{tir,i\max}}, \qquad \text{(B-7)}$$

where i is the subscripts s, t, or g, depending on the selected category. $E_{tir,i\max}$ is maximum emission energy in the selected category. If the equation (B-7) meets a given α, the position was selected. If the equation (B-7) did not meet a given α, the selected position was rejected and a new position was determined by random numbers.

The directions of emission $\Omega_E(\theta_E, \phi_E)$ were determined to follow the angular distribution of emission of trees and the soil elements as well as by the incoming radiation from the sky. We assumed that the emissions from the sky and the ground surface followed Lambert's cosine law. Directions of emission from the soil and incoming radiation from the sky were calculated by the same equation as the scattering case, using two random numbers (α_θ, α_ϕ):

$$\theta_E = \frac{1}{2}\arccos(1-2\alpha_\theta) \qquad \text{for sky} \qquad \text{(B-8a)}$$

$$\theta_E = \frac{1}{2}\{\pi + \arccos(1-2\alpha_\theta)\} \qquad \text{for ground} \qquad \text{(B-8b)}$$

$$\phi_E = 2\pi\alpha_\phi \qquad \text{(B-8c)}$$

On the leaf and woody surfaces, we also assumed that the emissions follow Lambert's cosine law relative to the normal direction of leaf and woody surface. Therefore, the emission had to be determined relative to given normal vectors $\Omega_L(\theta_L, \phi_L)$ of the leaves and woody materials. We determined emission vectors by two steps. First, normal vectors of leaves and woody elements were randomly selected using two random numbers. Then we applied the rejection technique to the selection or rejection of randomly selected normal vectors. In θ_E direction, the following criterion was applied:

996 $\alpha < g_L(\theta_L(\alpha_\theta))$, (B-9)

997

998 where g_L is a leaf or woody angle distribution and α_0 is a random number. Azimuth
999 direction ϕ_L was automatically selected when θ_L direction was determined as we
1000 assumed the random distribution to the azimuth direction.

1001 In the second step, the direction of emission relative to leaf or woody normal
1002 was determined using the same equations (B-8a-c). Emission occurs both from the
1003 surface of adaxial and abaxial sides. Assuming that the temperatures of the adaxial and
1004 abaxial sides were identical, either the adaxial or the abaxial side was randomly selected.
1005 Finally, $\Omega_E(\theta_E, \phi_E)$ was obtained by a coordinate transformation from the emission
1006 direction relative to the leaf or woody normal.

1007

1008

Acknowledgment

The first author was financially supported by the Postdoctoral Fellowship for Research Abroad of Japan Society for the Promotion of Science. The project was supported by the Office of Science (BER) of the U.S. Department of Energy (DE-FG02-03ER63638 and DE-SC0005130). We thank Joseph Verfaillie for providing constructive comments.

References

Antyufeev, V.S. and Marshak, A.L., 1990. Monte-Carlo Method and Transport-Equation in Plant Canopies. Remote Sensing of Environment, 31(3): 183-191.

Asner, G.P., Wessman, C.A. and Archer, S., 1998. Scale dependence of absorption of photosynthetically active radiation in terrestrial ecosystems. Ecological Applications, 8(4): 1003-1021.

Baldocchi, D., 1994. An Analytical Solution for Coupled Leaf Photosynthesis and Stomatal Conductance Models. Tree Physiology, 14(7-9): 1069-1079.

Baldocchi, D., 1997. Measuring and modelling carbon dioxide and water vapour exchange over a temperate broad-leaved forest during the 1995 summer drought. Plant Cell and Environment, 20(9): 1108-1122.

Baldocchi, D. and Meyers, T., 1998. On using eco-physiological, micrometeorological and biogeochemical theory to evaluate carbon dioxide, water vapor and trace gas fluxes over vegetation: a perspective. Agricultural and Forest Meteorology, 90(1-2): 1-25.

Baldocchi, D.D. and Harley, P.C., 1995. Scaling Carbon-Dioxide and Water-Vapor Exchange from Leaf to Canopy in a Deciduous Forest .2. Model Testing and Application. Plant Cell and Environment, 18(10): 1157-1173.

Baldocchi, D.D. and Wilson, K.B., 2001. Modeling CO2 and water vapor exchange of a temperate broadleaved forest across hourly to decadal time scales. Ecological Modelling, 142(1-2): 155-184.

Baldocchi, D.D., Xu, L.K. and Kiang, N., 2004. How plant functional-type, weather, seasonal drought, and soil physical properties alter water and energy fluxes of an oak-grass savanna and an annual grassland. Agricultural and Forest Meteorology, 123(1-2): 13-39.

Ball, J.T., 1988. An analysis of stomata1 conductance, Stanford University, CA, 89 pp.

Brutsaert, W., 1975. Derivable Formula for Long-Wave Radiation from Clear Skies. Water Resources Research, 11(5): 742-744.

Campbell, G., 1985. Soil physics with basic. Transport models for soil-plant systems, 150. Elsevier.

Cescatti, A., 1997a. Modelling the radiative transfer in discontinuous canopies of asymmetric crowns. I. model structure and algorithms. Ecological Modelling, 100(2/3): 263-274.

Cescatti, A., 1997b. Modelling the radiative transfer in discontinuous canopies of asymmetric crowns. II. Model testing and application in a Norway spruce stand. Ecological

1049 Modelling, 100(2/3): 275-284.
1050 Chen, Q., 2009. Improvement of the Edge-based Morphological (EM) method for lidar data
1051 filtering. International Journal of Remote Sensing, 30(4): 1069-1074.
1052 Chen, Q., Baldocchi, D., Gong, P. and Dawson, T., 2008. Modeling radiation and
1053 photosynthesis of a heterogeneous savanna woodland landscape with a hierarchy of
1054 model complexities. Agricultural and Forest Meteorology, 148(6-7): 1005-1020.
1055 Chen, Q., Baldocchi, D., Gong, P. and Kelly, M., 2006. Isolating individual trees in a savanna
1056 woodland using small footprint lidar data. Photogrammetric Engineering and Remote
1057 Sensing, 72(8): 923-932.
1058 Chen, Q., Gong, P., Baldocchi, D. and Tian, Y.Q., 2007a. Estimating basal area and stem
1059 volume for individual trees from lidar data. Photogrammetric Engineering and Remote
1060 Sensing, 73(12): 1355-1365.
1061 Chen, Q., Gong, P., Baldocchi, D. and Xie, G., 2007b. Filtering airborne laser scanning data
1062 with morphological methods. Photogrammetric Engineering and Remote Sensing,
1063 73(2): 175-185.
1064 Disney, M. et al., 2010, Simulating the impact of discrete-return lidar system and survey
1065 characteristics over young conifer and broadleaf forests, Remote Sensing of
1066 Environment, 114: 1546-1560.
1067 Gamon, J.A., Cheng, Y.F., Claudio, H., MacKinney, L. and Sims, D.A., 2006. A mobile tram
1068 system for systematic sampling of ecosystem optical properties. Remote Sensing of
1069 Environment, 103(3): 246-254.
1070 Gastellu-Etchegorry, J.P., 2008. 3D modeling of satellite spectral images, radiation budget and
1071 energy budget of urban landscapes. Meteorology and Atmospheric Physics, 102(3-4):
1072 187-207.
1073 Gutschick, V., 1990. Joining leaf photosynthesis models and canopy photon-transport models.
1074 Springer-Verlag.
1075 Hutchison, B. A. et al. 1980, Effects of Sky Brightness Distribution Upon Penetration of
1076 Diffuse-Radiation through Canopy Gaps in a Deciduous Forest, Agricultural
1077 Meteorology 22(2): 137-147.
1078 Haverd, V., Cuntz, M., Leuning, R. and Keith, H., 2007. Air and biomass heat storage fluxes in
1079 a forest canopy: Calculation within a soil vegetation atmosphere transfer model.
1080 Agricultural and Forest Meteorology, 147(3-4): 125-139.
1081 Hosoi, F. and Omasa, K., 2007. Factors contributing to accuracy in the estimation of the woody

canopy leaf area density profile using 3D portable lidar imaging. Journal of Experimental Botany, 58(12): 3463-3473.

Hopkinson, C., 2007, The influence of flying altitude, beam divergence, and pulse repetition frequency on lase pulse return intensity and canopy frequency distribution, Canadian Journal of Remote Sensing, 33(4): 321-324.

Ichii, K. et al., 2010. Multi-model analysis of terrestrial carbon cycles in Japan: limitations and implications of model calibration using eddy flux observations. Biogeosciences, 7(7): 2061-2080.

Kim, J. et al., 2006. Upscaling fluxes from tower to landscape: Overlaying flux footprints on high-resolution (IKONOS) images of vegetation cover. Agricultural and Forest Meteorology, 136(3-4): 132-146.

Kobayashi, H. and Iwabuchi, H., 2008. A coupled 1-D atmosphere and 3-D canopy radiative transfer model for canopy reflectance, light environment, and photosynthesis simulation in a heterogeneous landscape. Remote Sensing of Environment, 112(1): 173-185.

Kucharik, C.J., Norman, J.M. and Gower, S.T., 1998. Measurements of branch area and adjusting leaf area index indirect measurements. Agricultural and Forest Meteorology, 91(1-2): 69-88.

Law, B.E., Cescatti, A. and Baldocchi, D.D., 2001. Leaf area distribution and radiative transfer in open-canopy forests: implications for mass and energy exchange. Tree Physiology, 21(12-13): 777-787.

Lindroth, A., Molder, M. and Lagergren, F., 2010. Heat storage in forest biomass improves energy balance closure. Biogeosciences, 7(1): 301-313.

Ma, S., Baldocchi, D.D., Mambelli, S. and Dawson, T.E., 2011. Are temporal variations of leaf traits responsible for seasonal and inter-annual variability in ecosystem CO2 exchange? Functional Ecology, 25(1): 258-270.

Ma, S.Y., Baldocchi, D.D., Xu, L.K. and Hehn, T., 2007. Inter-annual variability in carbon dioxide exchange of an oak/grass savanna and open grassland in California. Agricultural and Forest Meteorology, 147(3-4): 157-171.

Macfarlane, C. et al., 2007. Estimation of leaf area index in eucalypt forest using digital photography. Agricultural and Forest Meteorology, 143(3-4): 176-188.

Mahecha, M. D., et al., 2010, Comparing observations and process- based simulations of biosphere- atmosphere exchanges on multiple timescales, Journal of Geophysical Research, 115, G02003, doi:10.1029/2009JG001016.

1115 Malenovsky, Z. et al., 2008. Influence of woody elements of a Norway spruce canopy on nadir
1116 reflectance simulated by the DART model at very high spatial resolution. Remote
1117 Sensing of Environment, 112(1): 1-18.
1118 Marchuk, G., G. Mikhailov, M. Nazaraliev, R. Darbinjan, B. Kargin, and B. Elepov, 1980. The
1119 Monte Carlo Methods in Atmospheric Optics. Springer-Verlag.
1120 Medlyn, B., 2004. A MAESTRO Retrospective. Forests at the Land-Atmosphere Interface.
1121 CABI Publishing.
1122 Morales, P. et al., 2005. Comparing and evaluating process-based ecosystem model predictions
1123 of carbon and water fluxes in major European forest biomes. Global Change Biology,
1124 11(12): 2211-2233.
1125 Norman, J.M. and Welles, J.M., 1983. Radiative-Transfer in an Array of Canopies. Agronomy
1126 Journal, 75(3): 481-488.
1127 North, P.R.J., 1996. Three-dimensional forest light interaction model using a Monte Carlo
1128 method. Ieee Transactions on Geoscience and Remote Sensing, 34(4): 946-956.
1129 Paw U, K.T., 1987. Mathematical-Analysis of the Operative Temperature and Energy Budget.
1130 Journal of Thermal Biology, 12(3): 227-233.
1131 Pinty, B. et al., 2001. Radiation transfer model intercomparison (RAMI) exercise. Journal of
1132 Geophysical Research-Atmospheres, 106(D11): 11937-11956.
1133 Pinty, B. et al., 2004. Radiation Transfer Model Intercomparison (RAMI) exercise: Results
1134 from the second phase. Journal of Geophysical Research-Atmospheres, 109(D6): 19.
1135 Press, W.H., S. A. Teukolsky, W. T. Vetterling, and B. P. Flannery, 1992. Numerical Recipes in
1136 Fortran 77: The Art of Scientific Computing. Second Edition. Cambridge University
1137 Press, 933 pp.
1138 Ryu, Y. et al., 2010a. How to quantify tree leaf area index in an open savanna ecosystem: a
1139 multi-instrument and multi-model approach. Agricultural and Forest Meteorology,
1140 150(1): 63-76.
1141 Ryu, Y., et al., 2010b. On the correct estimation of effective leaf area index: does it reveal
1142 information on clumping effects? Agricultural and Forest Meteorology 150: 463-472.
1143 Sankaran, M. et al., 2005. Determinants of woody cover in African savannas. Nature,
1144 438(7069): 846-849.
1145 Scholes, R.J. and Archer, S.R., 1997. Tree-grass interactions in savannas. Annual Review of
1146 Ecology and Systematics, 28: 517-544.
1147 Schwalm, C. R., et al., 2010, A model- data intercomparison of CO2 exchange across North

America: Results from the North American Carbon Program site synthesis, Journal of Geophysical Research, 115, G00H05, doi:10.1029/2009JG001229.

Silberstein, R.P., Sivapalan, M., Viney, N.R., Held, A. and Hatton, T.J., 2003. Modelling the energy balance of a natural jarrah (Eucalyptus marginata) forest. Agricultural and Forest Meteorology, 115(3-4): 201-230.

Sinoquet, H. and Bonhomme, R., 1992. Modeling Radiative-Transfer in Mixed and Row Intercropping Systems. Agricultural and Forest Meteorology, 62(3-4): 219-240.

Sinoquet, H., Le Roux, X., Adam, B., Ameglio, T. and Daudet, F.A., 2001. RATP: a model for simulating the spatial distribution of radiation absorption, transpiration and photosynthesis within canopies: application to an isolated tree crown. Plant Cell and Environment, 24(4): 395-406.

Song, C. et al., 2009, Energy, water, and carbon fluxes in a loblolly pine stand: Results from uniform and gappy canopy models with comparisons to eddy flux data, Journal of Geophysical Research, 114, G04021, doi:10.1029/2009JG000951.

Tournebize, R. and Sinoquet, H., 1995. Light Interception and Partitioning in a Shrub/Grass Mixture. Agricultural and Forest Meteorology, 72(3-4): 277-294.

Verrelst, J., Schaepman, M.E., Malenovsky, Z. and Clevers, J., 2010. Effects of woody elements on simulated canopy reflectance: Implications for forest chlorophyll content retrieval. Remote Sensing of Environment, 114(3): 647-656.

Wang, Y.P. and Jarvis, P.G., 1990. Description and Validation of an Array Model - Maestro. Agricultural and Forest Meteorology, 51(3-4): 257-280.

Watanabe, T. and Ohtani, Y., 1998. A comparative study on calculation methods of heat conduction in tree stems. Journal of Agricultural Meteorology, 54(1): 47-54.

Widlowski, J.-L., 2010. On the bias of instantaneous FAPAR estimates in open-canopy forests. Agricultural and Forest Meteorology(150): 1501-1522.

Widlowski, J.L. et al., 2007. Third Radiation Transfer Model Intercomparison (RAMI) exercise: Documenting progress in canopy reflectance models. Journal of Geophysical Research-Atmospheres, 112(D9): 28.

Widlowski, J-L., et al., 2011, RAMI4PILPS: An Intercomparison of Formulations for the Partitioning of Solar Radiation in Land Surface Models, Journal of Geophysical Research, 116, G02019, doi:10.1029/2010JG001511.

Wilson, K. et al., 2002. Energy balance closure at FLUXNET sites. Agricultural and Forest Meteorology, 113(1-4): 223-243.

1181 Xu, L.K. and Baldocchi, D.D., 2003. Seasonal trends in photosynthetic parameters and stomatal
1182 conductance of blue oak (Quercus douglasii) under prolonged summer drought and high
1183 temperature. Tree Physiology, 23(13): 865-877.
1184 Zande, D.v.d. et al., 2009. 3D upscaling of transpiration from leaf to tree using ground-based
1185 LiDAR: application on a Mediterranean Holm oak (Quercus ilex L.) tree. Agricultural
1186 and Forest Meteorology, 149(10): 1573-1583.
1187
1188
1189
1190

Table

Table 1. Forest structural and physiological parameters used in the simulation

	Canopy reflectance (Nadir view BRF)		**Radiation budget (Understory)**					**Radiation budget (Top of the canopy)**			
Data source	AVIRIS		Traversing radiometer system				Spectral Transmittance	Flux tower measurement			
Date (Day of the year)	5/12/2006 (132)	8/5/2007 (217)	5/3/2008 (124)	5/9/2008 (130)	7/12/2008, (194)	8/2/2008 (215)	8/28/2009 (240)	3/8/2008-3/14/2008 (68-74)	4/24/2008-5/4/2008 (115-121)	7//6/2008-7/12/2008 (188-194)	7/18/2008 -7/28/2008 (204-210)
Area (Fig. 3)	No. 1	No. 1	No. 3	No. 3	No. 3	No. 3	No. 3	No. 2	No. 2	No. 2	No. 2
Leaf area density	0.52	0.52	0.52	0.52	0.52	0.52	0.52	0.0	0.52	0.52	0.52
Woody area density	0.56	0.56	0.56	0.56	0.56	0.56	0.56	0.56	0.56	0.56	0.56
Leaf angle distribution (tree)	Erectrophile	Erectrophile	Erectrophile	Erectrophile	Erectrophile	Erectrophile	Erectrophile	Erectrophile	Erectrophile	Erectrophile	Erectrophile
Branch angle distribution	Spherical	Spherical	Spherical	Spherical	Spherical	Spherical	Spherical	Spherical	Spherical	Spherical	Spherical
Grass LAI	1.08	0.00	0.60	0.00	0.00	0.00	0.00	0.81	0.71	0.0	0.00
Leaf angle distribution (grass)	Erectrophile	Erectrophile	Erectrophile	Erectrophile	Erectrophile	Erectrophile	Erectrophile	Erectrophile	Erectrophile	Erectrophile	Erectrophile
V_{cmax} (μmol m^{-2} s^{-1})	-	-	98.8	98.8	65.4	65.4	-	98.8	98.8	65.4	65.4
J_{max} (μmol m^{-2} s^{-1})	-	-	210.3	210.3	93.4	93.4	-	210.3	210.3	93.4	93.4
Soil water content at surface (m3 m-3)	-	-	0.115	0.098	0.065	0.065	-	0.318	0.115	0.065	0.065

Table 2. Spectral reflectance, transmittance, and emissivity of oak leaf, grass, woody elements, ground, bare soil.

		PAR	NIR	TIR	450nm	550nm	650nm	780nm	900nm
Blue Oak leaf	ρ	0.085 (0.005)	0.282 (0.013)	0.02	0.077 (0.020)	0.123 (0.009)	0.075 (0.007)	0.513 (0.027)	0.510 (0.056)
	τ	0.028 (0.004)	0.251 (0.007)	0.00	0.008 (0.017)	0.072 (0.009)	0.022 (0.006)	0.441 (0.016)	0.459 (0.048)
	ε	-	-	0.98	-	-	-	-	-
Grass	ρ	0.090 (0.001)	0.306 (0.007)	0.02	0.067 (0.014)	0.157 (0.021)	0.072 (0.007)	0.534 (0.014)	0.499 (0.041)
	τ	0.065 (0.012)	0.270 (0.019)	0.00	0.018 (0.016)	0.157 (0.022)	0.046 (0.012)	0.455 (0.023)	0.455 (0.043)
	ε	-	-	0.98	-	-	-	-	-
Woody elements	ρ	0.171 (0.040)	0.343 (0.05)	0.02	0.127 (0.016)	0.170 (0.0087)	0.218 (0.013)	0.299 (0.021)	0.377 (0.026)
	ε	-	-	0.98	-	-	-	-	-
Ground*	ρ	0.105 (0.044)	0.253 (0.037)	0.98	0.055 (0.012)	0.102 (0.022)	0.156 (0.030)	0.225 (0.039)	0.276 (0.046)
	ε	-	-	0.98	-	-	-	-	-
Bare soil	ρ	-	-	-	0.033	0.065	0.108	0.170	0.220

ρ: reflectance, τ: transmittance. Standard deviations are shown in the brackets.

PAR: 0.4-0.7μm, NIR: 0.7-4.0 μm

*The ground is a mixture of the soil and dead leaves.

Table 3. Statistics of the comparison between the simulated (3D scheme) and measured downward PAR, upward PAR, and net radiation (R_n) at the understory level along the rail track. Positive biases indicate that the simulated results are higher than the measurements.

	Slope	Intercept	r^2	RMSE	Bias
Downward PAR	0.99	68.25	0.97	136.79	65.93
Outgoing PAR	0.70	12.18	0.90	29.66	-15.87
R_n	0.88	15.25	0.95	56.95	-14.14

RMSE: root mean square error. The RMSE and bias unit for downward and outgoing PAR are μmol m^{-2} s^{-1}, and for R_n are W m^{-2}

Table 4. Statistics of the 3D model results of net radiation (R_n), sensible heat (H), latent hear (λE), the ground heat (G), tree photosynthesis (P_s), and PAR albedo. Positive biases indicate that the simulated results are higher than the measurements.

	Slope	Intercept	R^2	RMSE	Bias
R_n	1.06	31.70	0.99	52.00	40.38
H	1.20	-14.83	0.98	41.90	2.71
λE	1.53	5.26	0.96	40.60	23.05
G (soil)	1.46	-2.28	0.93	13.44	0.75
P_s (Tree only)	1.02	0.04	0.95	0.79	0.08
Albedo (PAR)	0.69	0.00	0.89	0.02	-0.01

RMSE: root mean square error. The unit of RMSE and bias for R_n, H, λE, G are W m^{-2}, and for P_s are μmol m^{-2} s^{-1}, and for PAR albedo are unitless.

Figure captions

Figure 1. Tree canopy structure assumed in this study (a) 3D scheme (b) 1D scheme.

Figure 2. Flowchart of the 3D radiation and energy balance model. Spatial distribution of PAR, NIR, and TIR radiations are computed by FLiES (Kobayashi and Iwabuchi, 2008). The spatial distributions of leaves and the soil temperature, which are required in the TIR simulation, are computed by the CANOAK scheme (Baldocchi and Meyers, 1998)

Figure 3. Left (AVIRIS image): The study site and spatial plots (1, 2, and 3) for the model evaluation. The size of 1, 2, and 3 are 600 by 600 m, 100 by 100 m, and 100 by 100 m, respectively. Right (IKONOS image): location of traverse radiometer system (the red line) and seven transects of digital cover photography (DCP). Yellow dots in the right images show the location of litterfall trap. The eddy covariance tower is located in the center of No. 2 (the red dot inside the yellow rectangle).

Figure 4. The measured (digital cover photography, DCP) and the simulated gap fractions along the transect F. LAD: leaf area density. The different LAD cases are shown in simulated gap fractions.

Figure 5. Visual comparisons of the simulated reflectance (red-green-blue composite, left) with AVIRIS data (right) for (a) May 12, 2006, at 10:22 PST (top), and (b) August 5, 2007 at 11:57 PST (bottom). The red-green-blue images were produced by histogram matching.

Figure 6. Comparisons of the spatially averaged canopy reflectances (bidirectional reflectance at the nadir view) of AVIRIS and 3D model in area No. 1 (Figure 3). The 1D model results are also shown. (a) May 12, 2006 and (b) August 5, 2007. Error bars for AVIRIS and 3D model cases show the standard deviation of canopy reflectance data across the scene.

Figure 7. Comparisons of the spatially averaged reflectances for (a) the crowns and (b) the understory parts in area No. 1. The simulated results are from the 3D scheme. Error bars show the standard deviation of bidirectional reflectance data across the scene.

Figure 8. Comparisons of the simulated canopy spectral transmittance (450 nm, 550 nm, 650 nm, 780 nm, and 900 nm) averaged over the transect A (T-A) and C (T-C), blue: 3D model with woody elements. Red: 3D model without woody elements, and green: 1D model with and without woody elements. For 1D simulation, we used an average LAI and WAI

around the transect A and C (LAI = 1.12, WAI=0.68).

Figure 9. Comparisons of the simulated and measured downward and upward PAR (PAR down and PAR up), and net radiation (R_n) along the transect of the traversing radiometer system at the woodland floor (DOY=194, 2008). (a) 10:00a.m. (b) 12:00p.m. (c)15:00p.m. The x axis is a distance from the west edge of the track.

Figure 10. The comparisons of simulated and measured diurnal patterns of downward PAR (PAR down), upward PAR (PAR up), and net radiation (R_n) at understory level (1m above the ground along the rail track). The PAR down, PAR up and R_n are averaged values over the rail track transect, and error bars are standard deviations along the rail track. Gaps on days 124 and 130 are due to missing data. (a) DOY 124 (b) DOY 130 (c) DOY 194 (d) DOY 215.

Figure 11. Diurnal patterns of simulated (red line: 3D scheme, blue line: 1D scheme) and measured (dots) net radiation (R_n), sensible heat (H), and latent heat flux (λE) densities. Four different periods in 2008 (DOY 68-75: non-foliated trees with active understory grasses, DOY115-121: fully foliated trees with active understory grasses, DOY 188-194 &204-210: fully foliated trees with dead understory grasses) are shown. The model was run in area No. 2, and measurements are 7-day averages of the eddy covariance data.

Figure 12. Comparison of measured and simulated (3D and 1D) energy fluxes in four different periods (DOY 68-75: non-foliated trees with active understory grasses, DOY115-121: fully foliated trees with active understory grasses, DOY 188-194 &204-210: fully foliated trees with dead understory grasses).

Figure 13. Diurnal patterns of fraction of absorbed PAR (FAPAR) and NIR (FANIR) by tree leaves, understory grasses and woody elements in four different periods ((a) DOY 68-75: non-foliated trees with active understory grasses, (b) DOY115-121: fully foliated trees with active understory grasses, (c) DOY 188-194 & (d) 204-210: fully foliated trees with dead understory grasses).

Figure 14. Upper figures: diurnal patterns of simulated (lines) and measured (dots) tree canopy photosynthesis (P_S). Three different periods in 2008 (DOY 68-75: non-foliated trees with active understory grasses, DOY115-121: fully foliated trees with active understory grasses, DOY 188-194 &204-210: fully foliated trees with dead understory grasses) are shown. Lower figures: the diurnal course of air temperature (T_{air}) and vapor pressure deficit (VPD). The model was run in area No. 2, and measurements are 7-day averages of the eddy covariance data. Photosynthesis of understory grasses is not included in P_S.

Figure 15. Comparison of measured and simulated (3D and 1D) tree canopy photosynthesis at three different periods (DOY115-121: fully foliated trees with active understory grasses, DOY 188-194 & 204-210: fully foliated trees with dead understory grasses).

Figure 16. Spatial variations of upward radiation fluxes (PAR, NIR, and TIR) and net radiation at three different heights (1 m: understory level, 12m: above the canopy, 23 m: eddy covariance tower height). The size of area is 100 by100 m and the eddy covariance tower is located at the center of the images. Spatial averages (Avg.) and standard deviations (STD) are also shown (unit: W m^{-2}). Simulation was performed at 12:00 PM, DOY115, 2008. The small blue dots on the TIR image at 1m level are the position of stem.

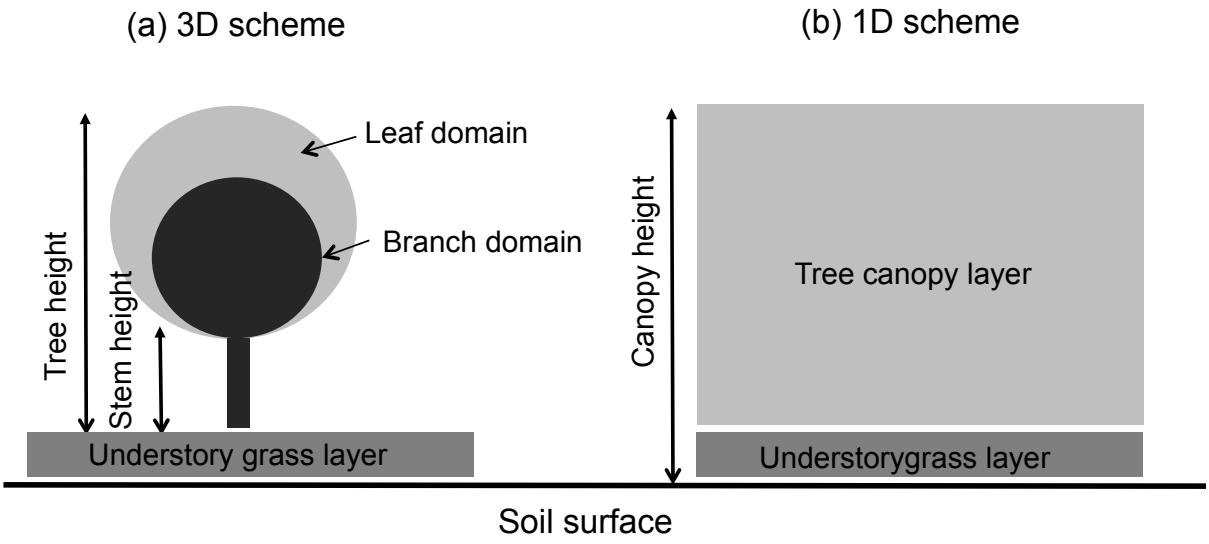

Figure 1. Tree canopy structure assumed in this study (a) 3D scheme (b) 1D scheme.

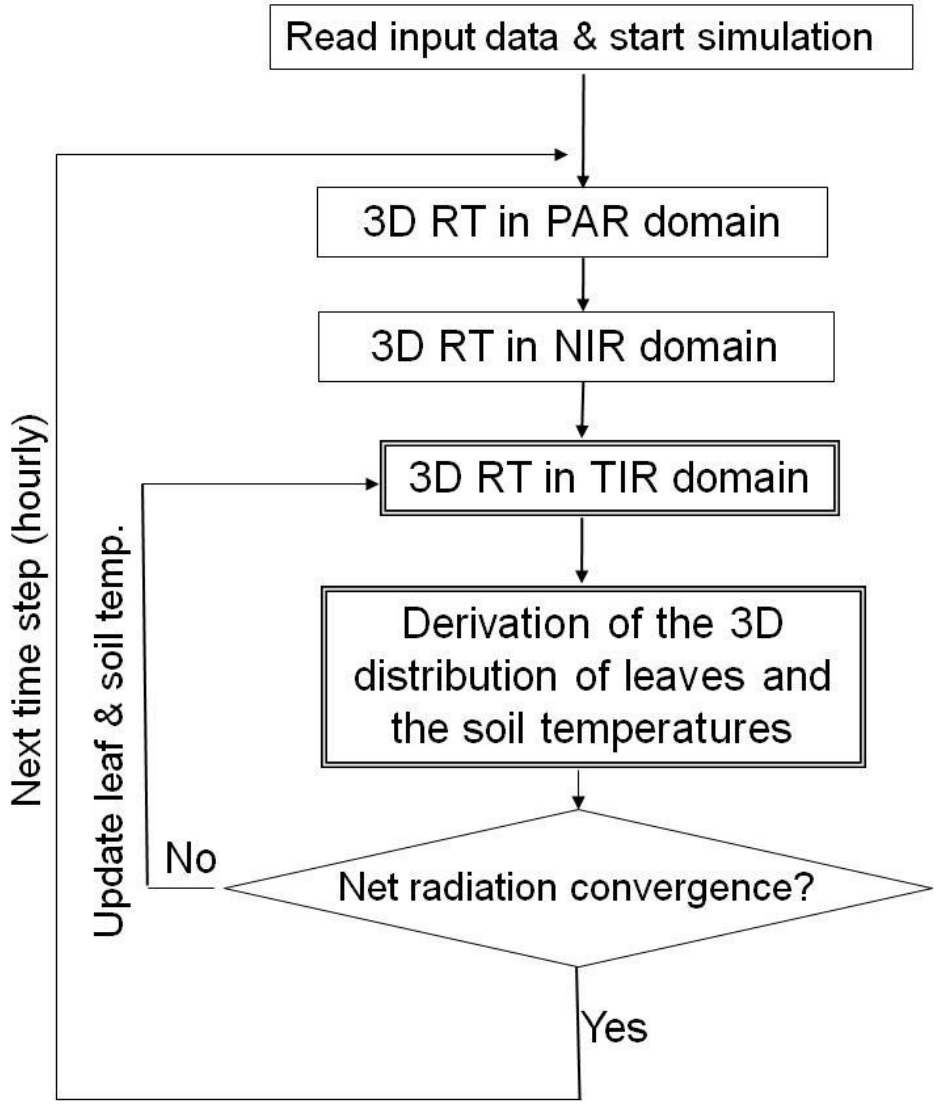

Figure 2. Flowchart of the 3D radiation and energy balance model. Spatial distribution of PAR, NIR, and TIR radiations are computed by FLiES (Kobayashi and Iwabuchi, 2008). The spatial distributions of leaves and the soil temperature, which are required in the TIR simulation, are computed by the CANOAK scheme (Baldocchi and Meyers, 1998).

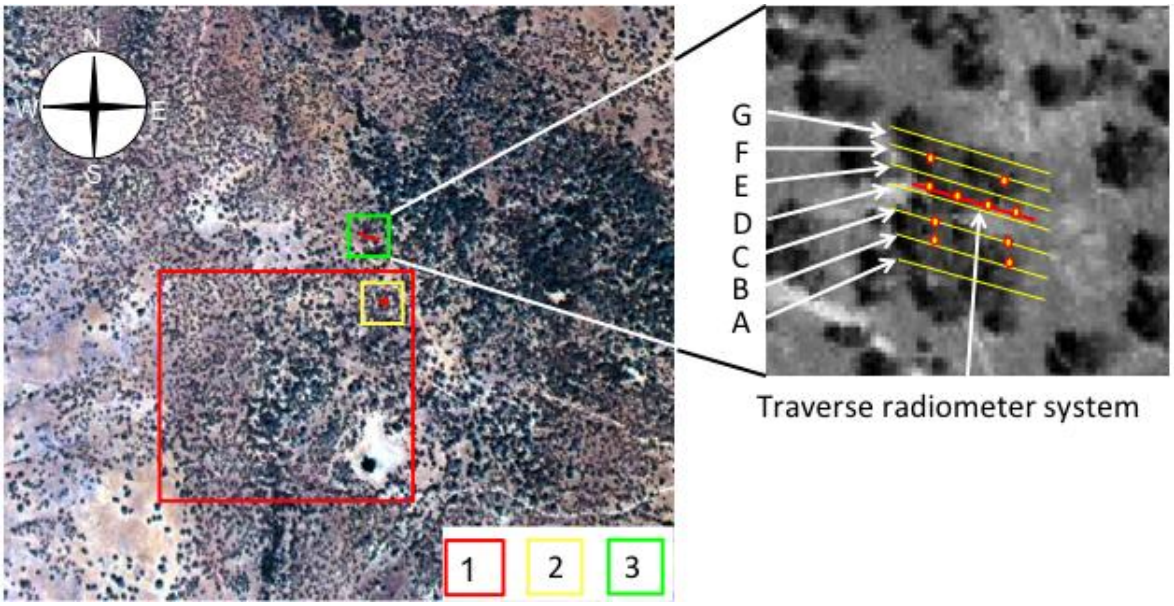

Figure 3. Left (AVIRIS image): The study site and spatial plots (1, 2, and 3) for the model evaluation. The size of 1, 2, and 3 are 600 by 600 m, 100 by 100 m, and 100 by 100 m, respectively. Right (IKONOS image): location of traverse radiometer system (the red line) and seven transects of digital cover photography (DCP). Yellow dots in the right images show the location of litterfall trap. The eddy covariance tower is located in the center of No. 2 (the red dot inside the yellow rectangle).

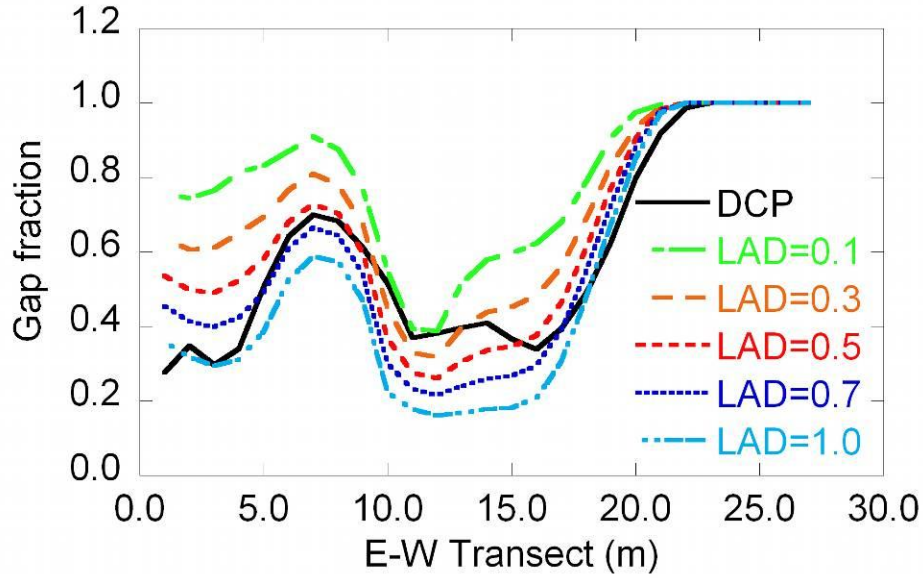

Figure 4. The measured (digital cover photography, DCP) and the simulated gap fractions along the transect F. LAD: leaf area density. The different LAD cases are shown in simulated gap fractions.

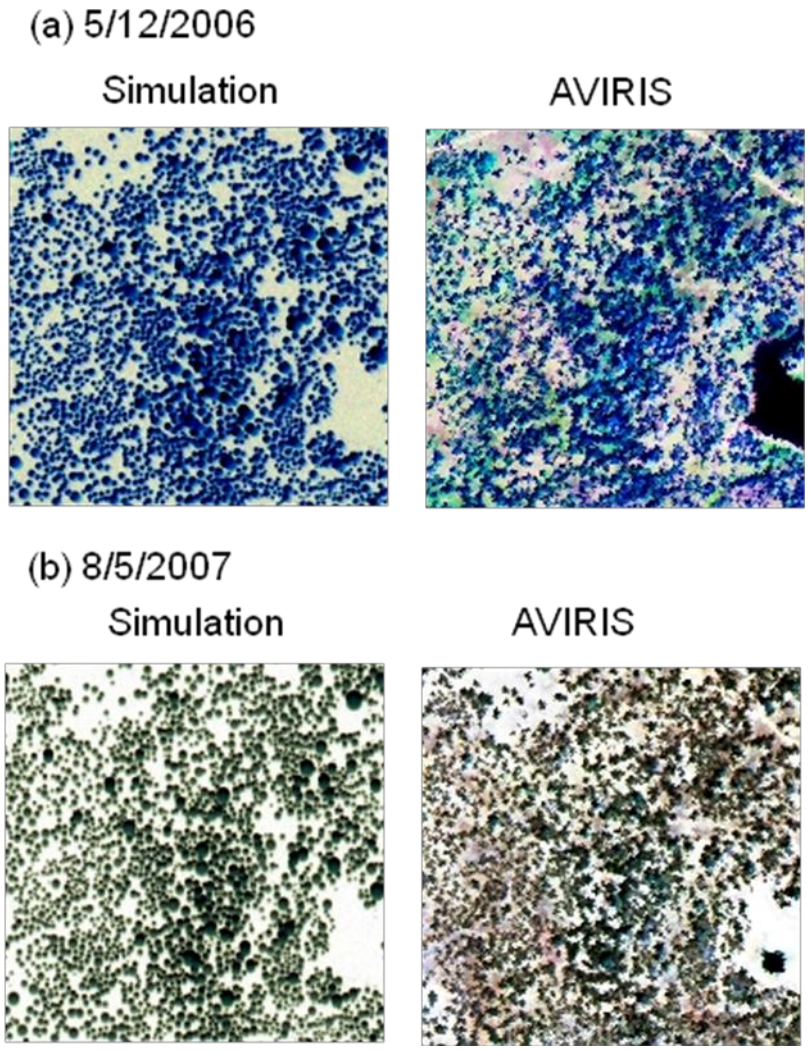

Figure 5. Visual comparisons of the simulated reflectance (red-green-blue composite, left) with AVIRIS data (right) for (a) May 12, 2006, at 10:22 PST (top), and (b) August 5, 2007 at 11:57 PST (bottom). The red-green-blue images were produced by histogram matching.

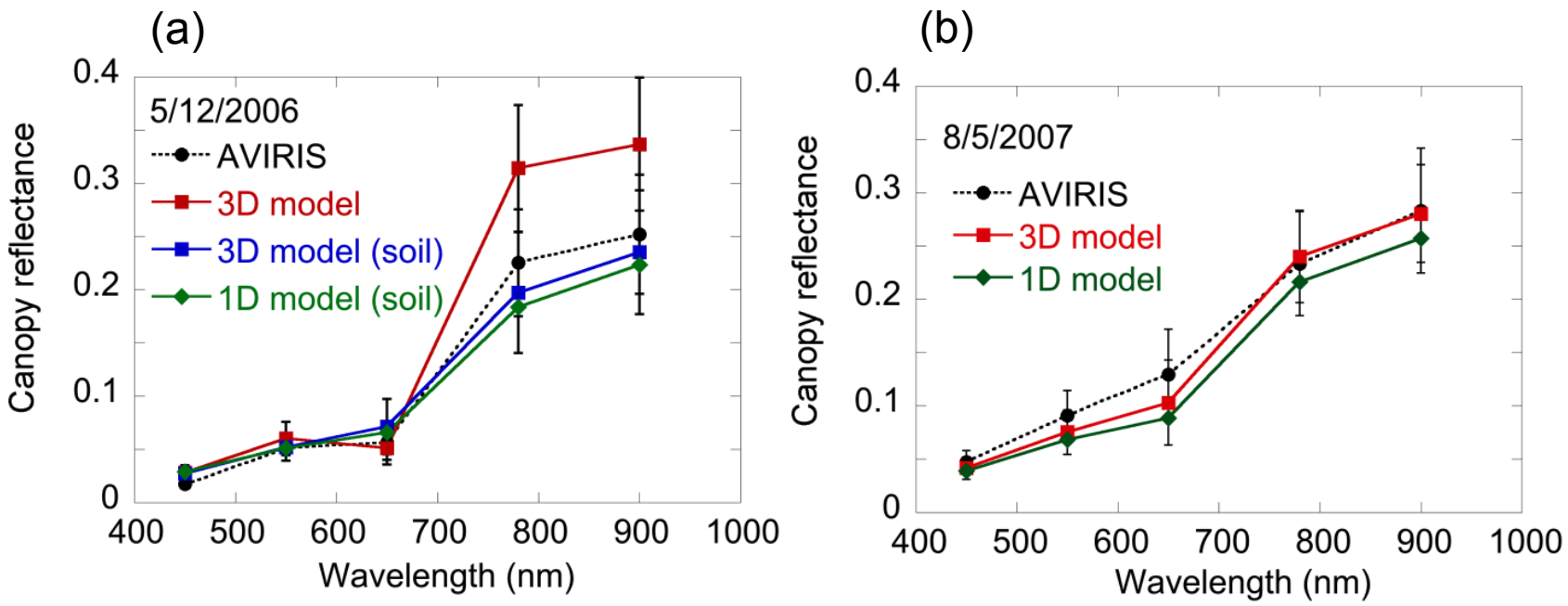

Figure 6. Comparisons of the spatially averaged canopy reflectances (bidirectional reflectance at the nadir view) of AVIRIS and 3D model in area No. 1 (Figure 3). The 1D model results are also shown. (a) May 12, 2006 and (b) August 5, 2007. Error bars for AVIRIS and 3D model cases show the standard deviation of canopy reflectance data across the scene.

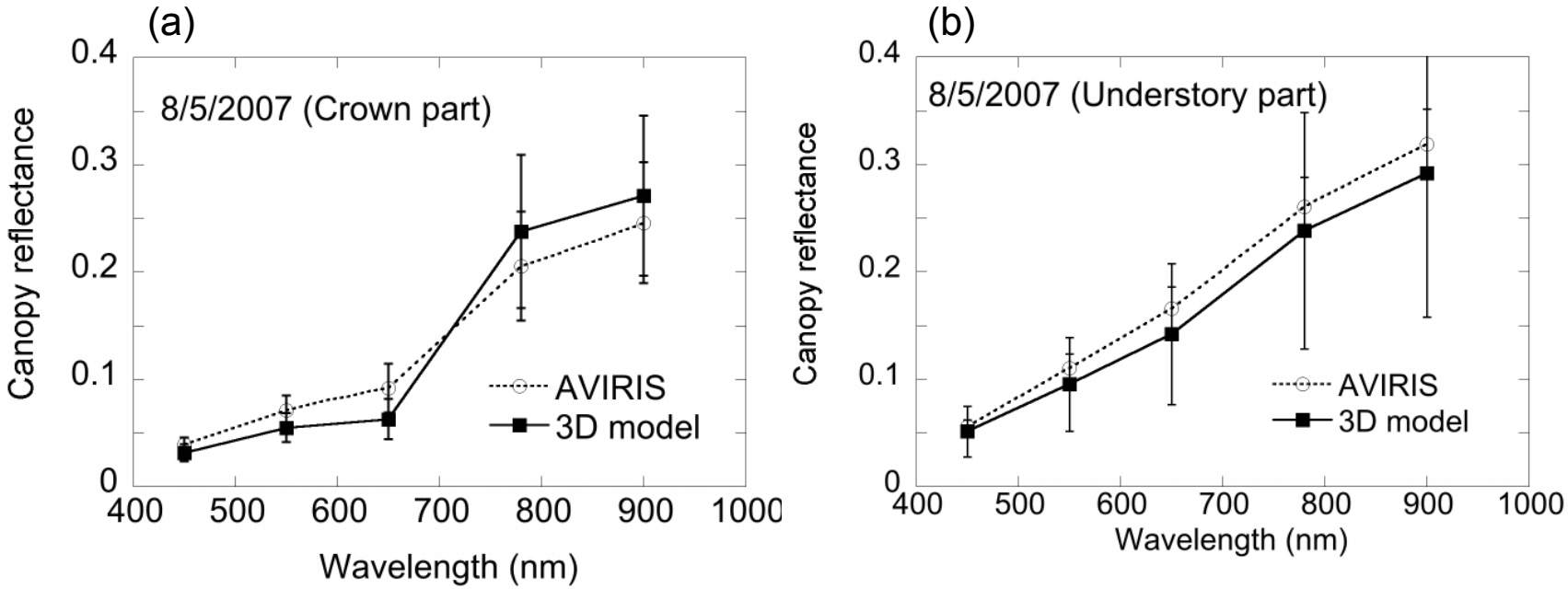

Figure 7. Comparisons of the spatially averaged reflectances for (a) the crowns and (b) the understory parts in area No. 1. The simulated results are from the 3D scheme. Error bars show the standard deviation of bidirectional reflectance data across the scene.

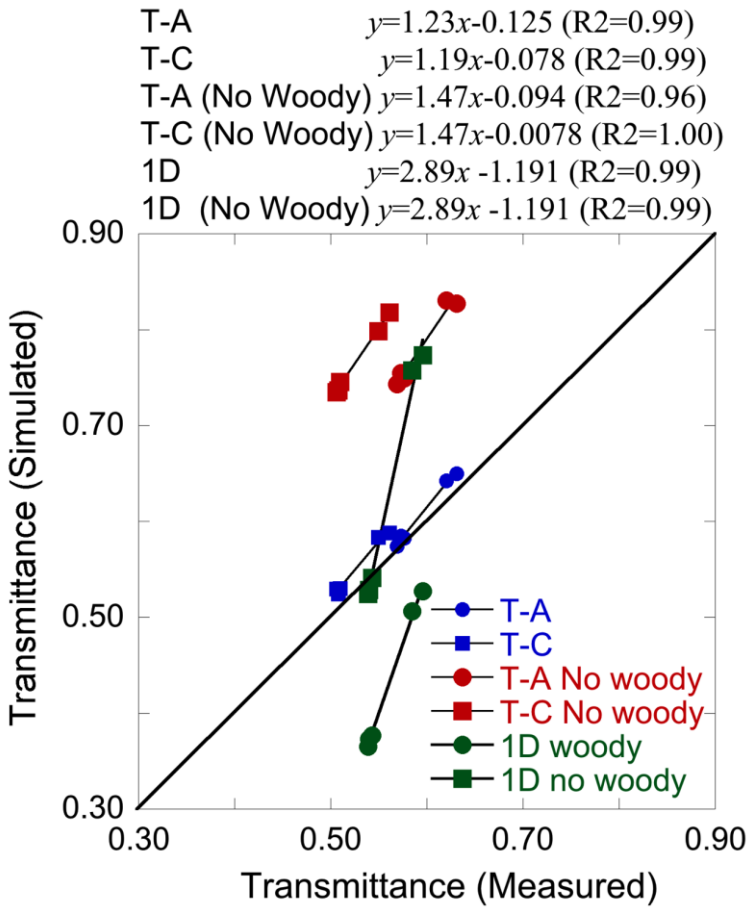

Figure 8. Comparisons of the simulated canopy spectral transmittance (450 nm, 550 nm, 650 nm, 780 nm, and 900 nm) averaged over the transect A (T-A) and C (T-C), blue: 3D model with woody elements. Red: 3D model without woody elements, and green: 1D model with and without woody elements. For 1D simulation, we used an average LAI and WAI around the transect A and C (LAI = 1.12, WAI=0.68).

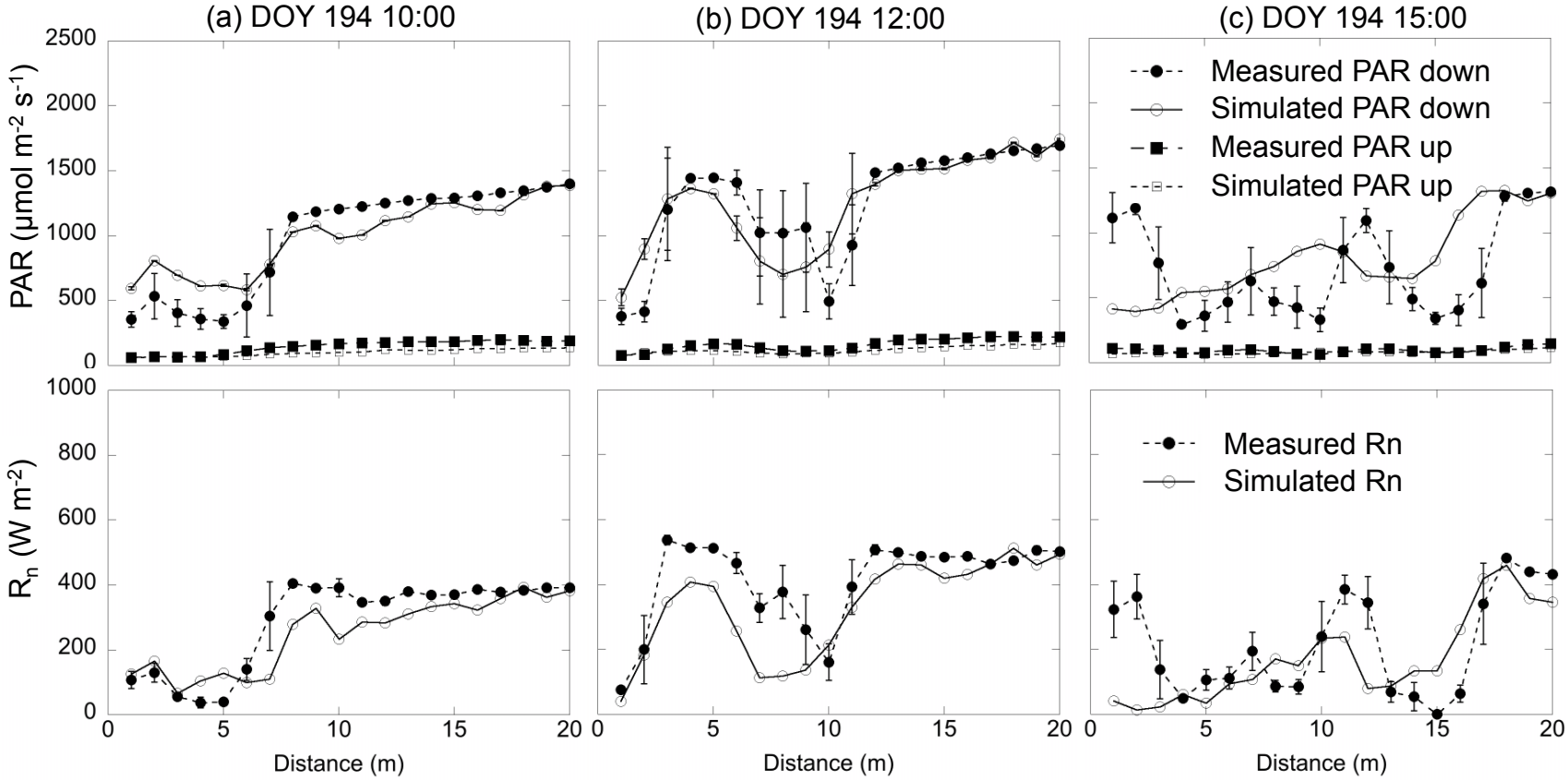

Figure 9. Comparisons of the simulated and measured downward and upward PAR (PAR down and PAR up), and net radiation (R_n) along the transect of the traversing radiometer system at the woodland floor (DOY=194, 2008). (a) 10:00a.m. (b) 12:00p.m. (c)15:00p.m. The *x* axis is a distance from the west edge of the track.

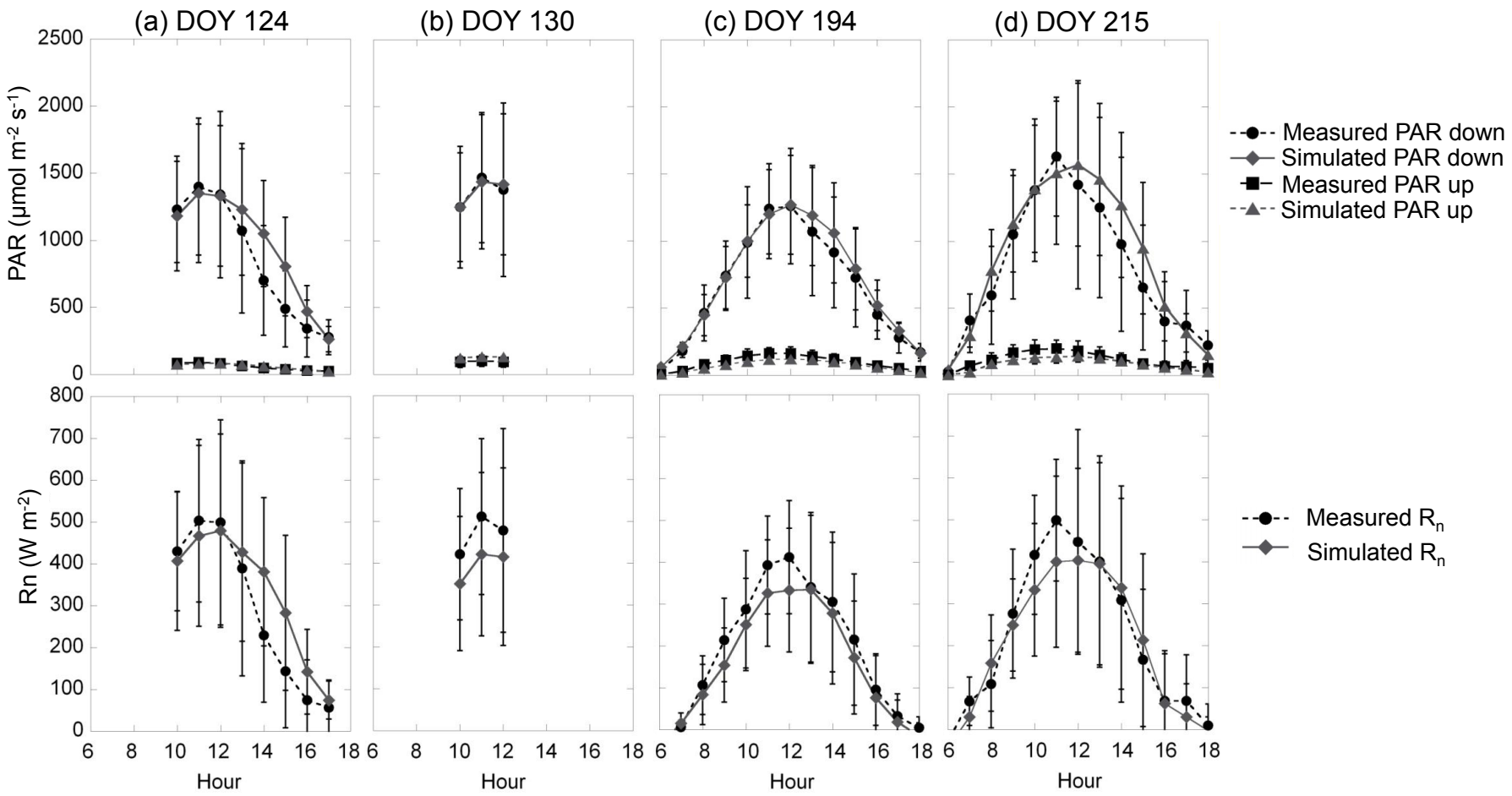

Figure 10. The comparisons of simulated and measured diurnal patterns of downward PAR (PAR down), upward PAR (PAR up), and net radiation (R_n) at understory level (1m above the ground along the rail track). The PAR down, PAR up and R_n are averaged values over the rail track transect, and error bars are standard deviations along the rail track. Gaps on days 124 and 130 are due to missing data. (a) DOY 124 (b) DOY 130 (c) DOY 194 (d) DOY 215.

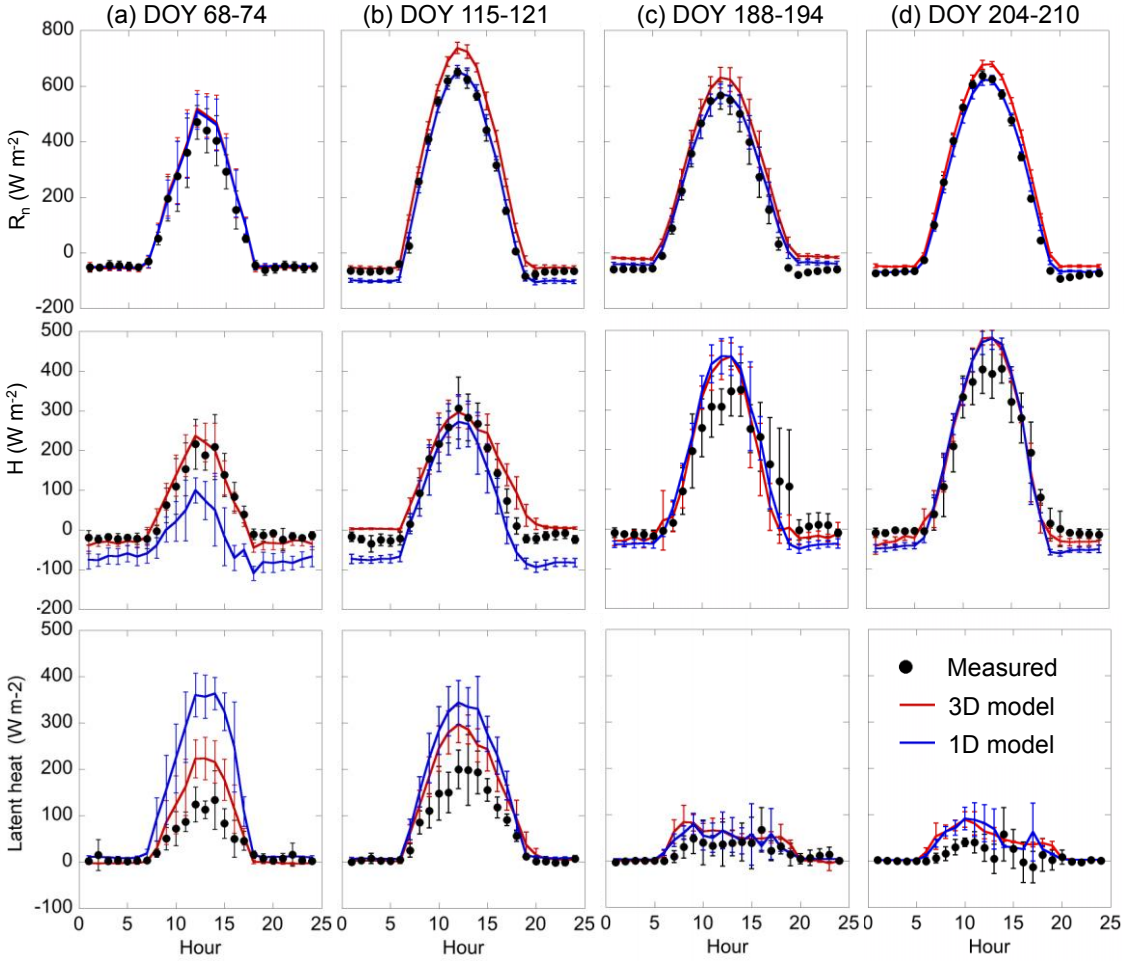

Figure 11. Diurnal patterns of simulated (red line: 3D scheme, blue line: 1D scheme) and measured (dots) net radiation (R_n), sensible heat (H), and latent heat flux (λE) densities. Four different periods in 2008 (DOY 68-75: non-foliated trees with active understory grasses, DOY115-121: fully foliated trees with active understory grasses, DOY 188-194 &204-210: fully foliated trees with dead understory grasses) are shown. The model was run in area No. 2, and measurements are 7-day averages of the eddy covariance data.

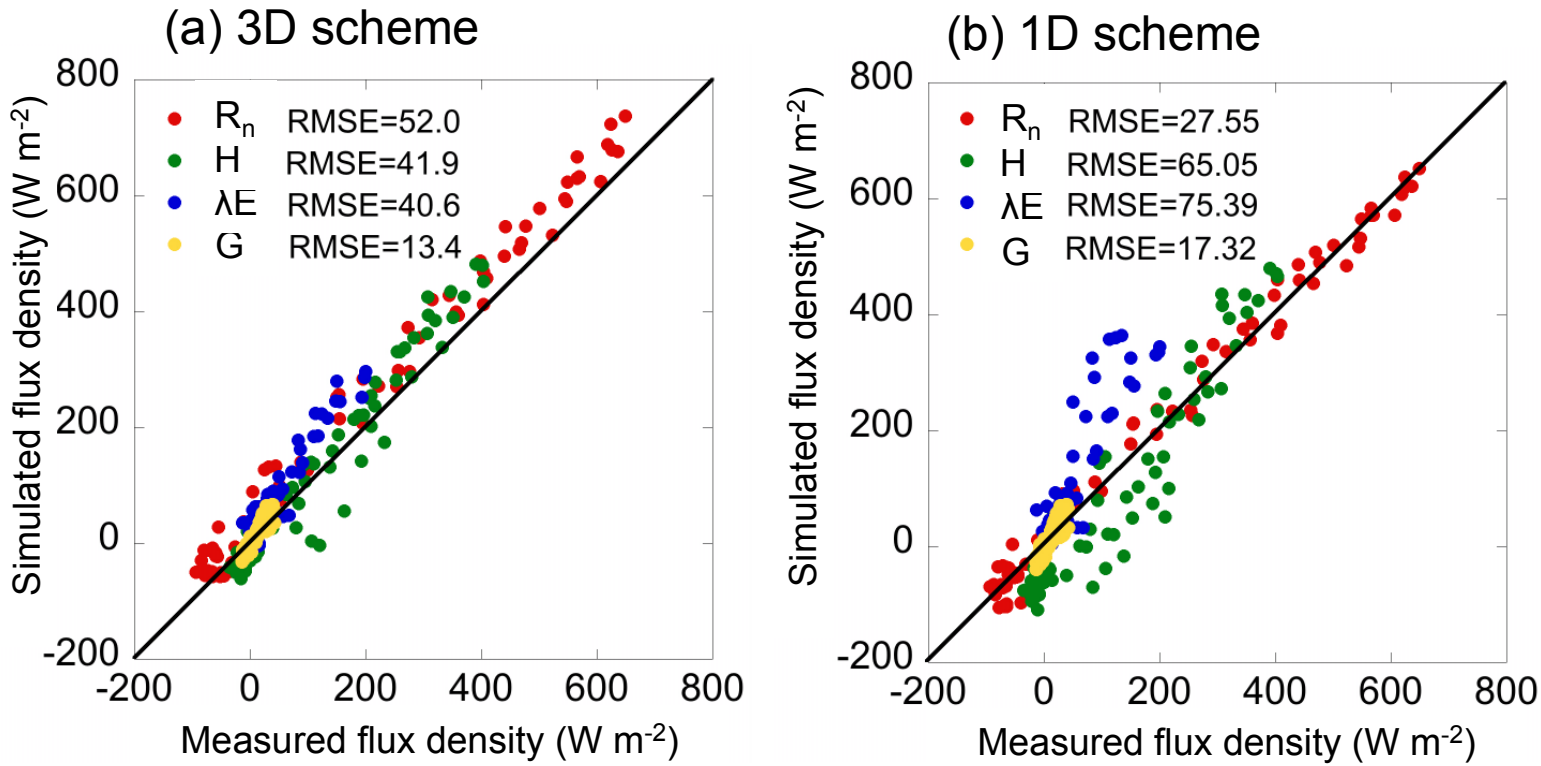

Figure 12. Comparison of measured and simulated (3D and 1D) energy fluxes in four different periods (DOY 68-75: non-foliated trees with active understory grasses, DOY115-121: fully foliated trees with active understory grasses, DOY 188-194 &204-210: fully foliated trees with dead understory grasses).

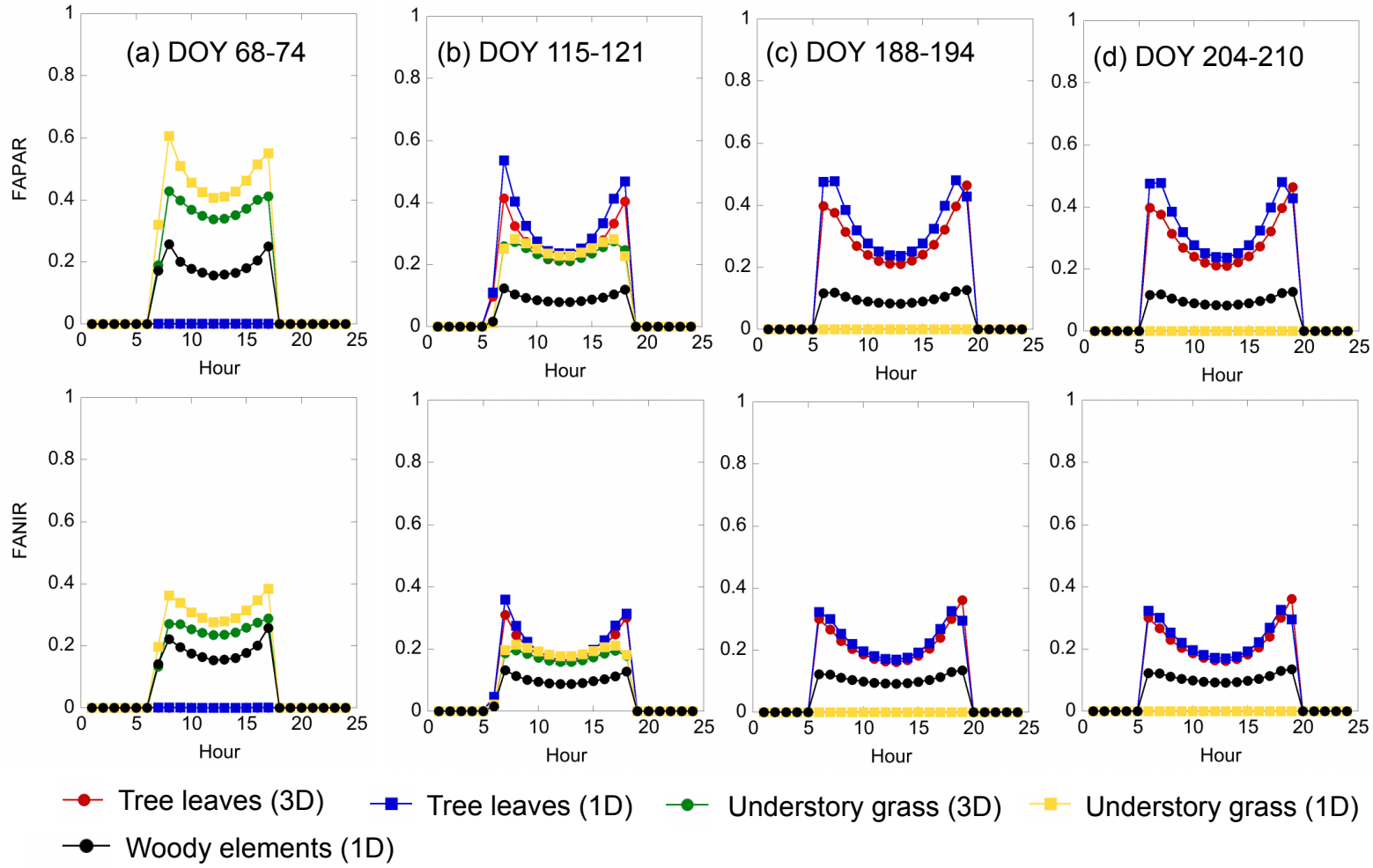

Figure 13. Diurnal patterns of fraction of absorbed PAR (FAPAR) and NIR (FANIR) by tree leaves, understory grasses and woody elements in four different periods ((a) DOY 68-75: non-foliated trees with active understory grasses, (b) DOY115-121: fully foliated trees with active understory grasses, (c) DOY 188-194 & (d) 204-210: fully foliated trees with dead understory grasses).

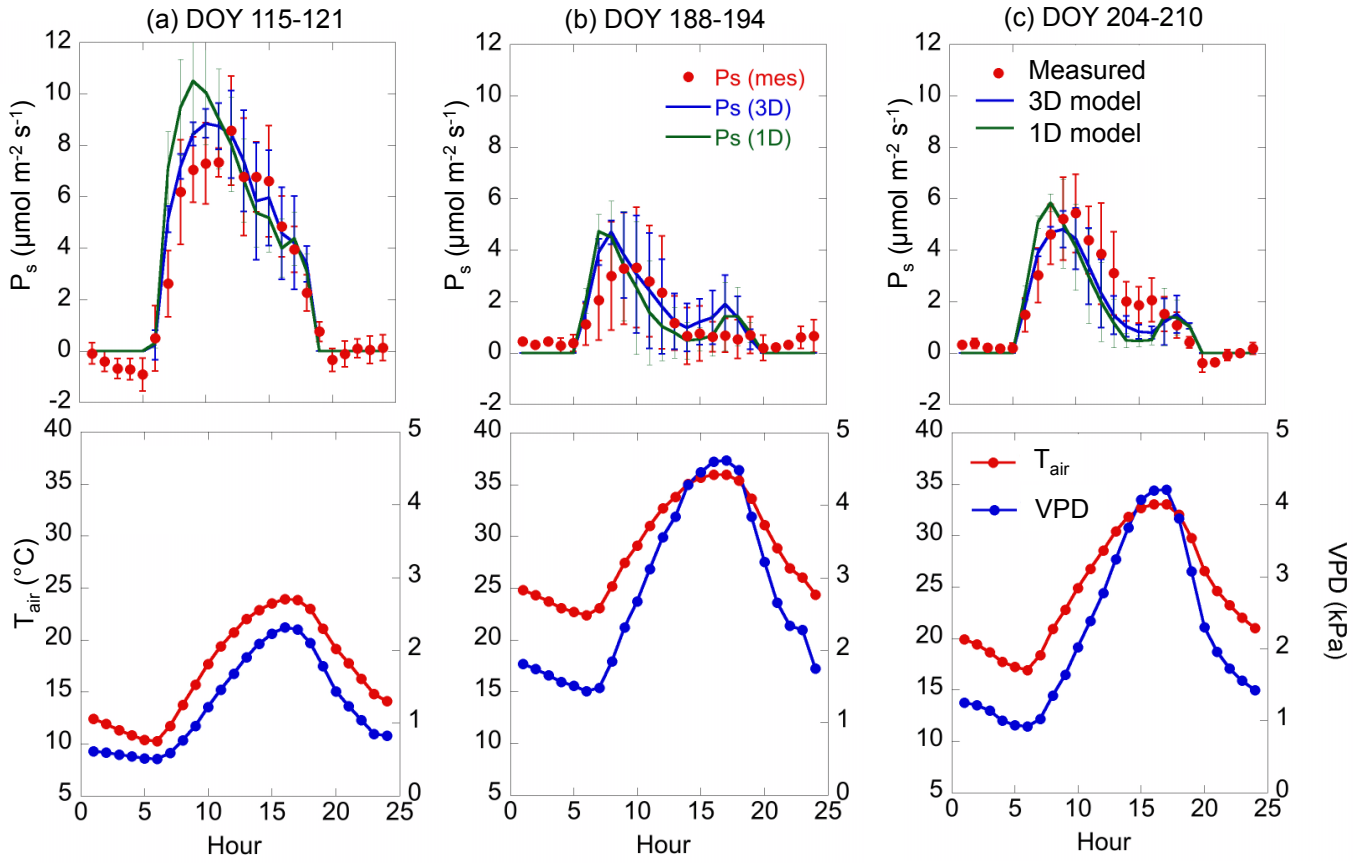

Figure 14. Upper figures: diurnal patterns of simulated (lines) and measured (dots) tree canopy photosynthesis (*P*s). Three different periods in 2008 (DOY 68-75: non-foliated trees with active understory grasses, DOY115-121: fully foliated trees with active understory grasses, DOY 188-194 &204-210: fully foliated trees with dead understory grasses) are shown. Lower figures: the diurnal course of air temperature (T_{air}) and vapor pressure deficit (VPD). The model was run in area No. 2, and measurements are 7-day averages of the eddy covariance data. Photosynthesis of understory grasses is not included in *P*s.

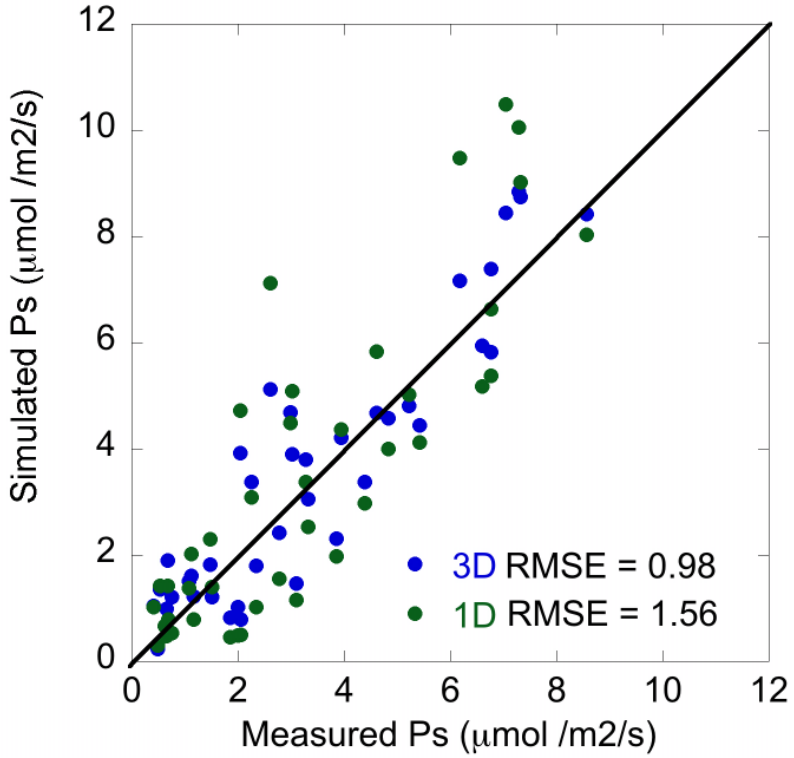

Figure 15. Comparison of measured and simulated (3D and 1D) tree canopy photosynthesis at three different periods (DOY115-121: fully foliated trees with active understory grasses, DOY 188-194 & 204-210: fully foliated trees with dead understory grasses).

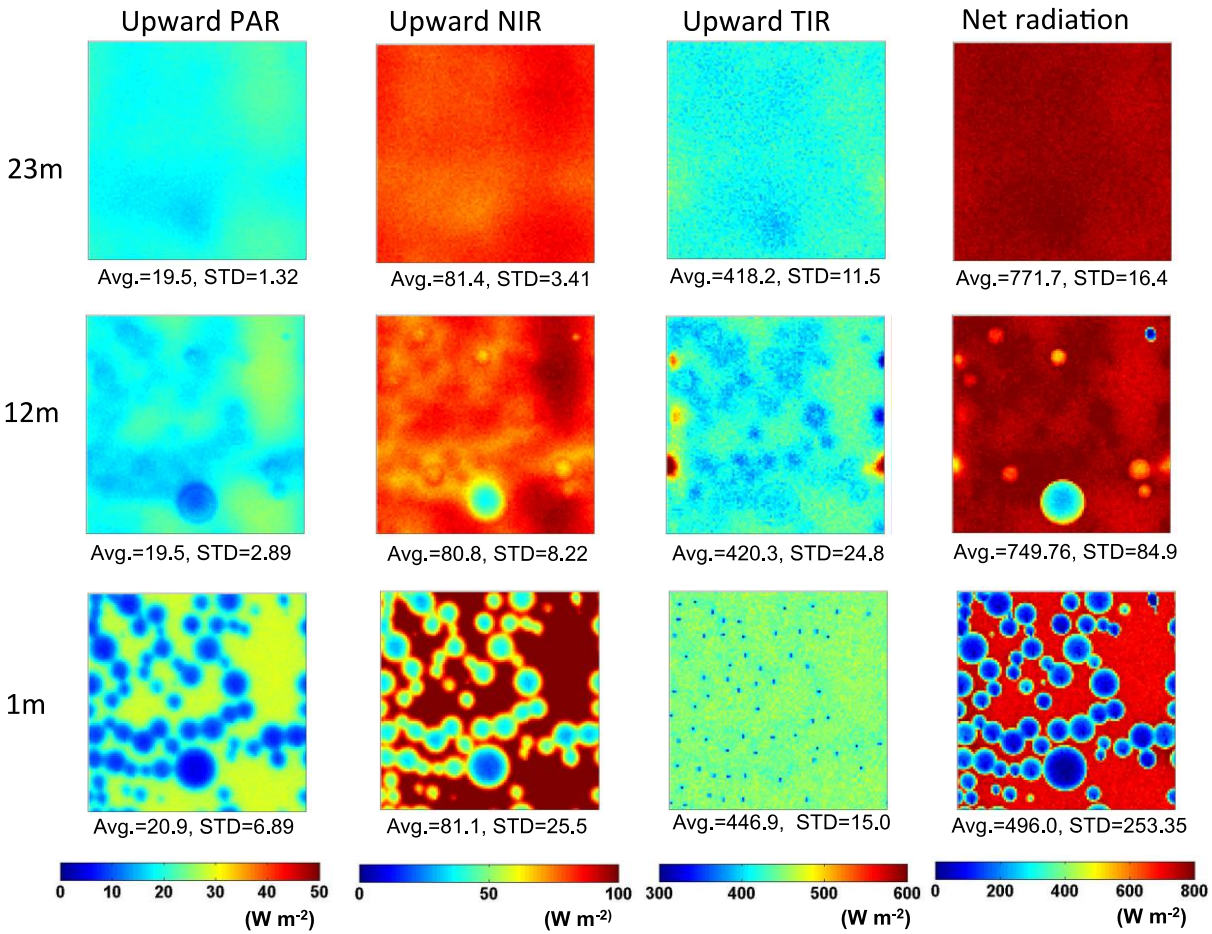

Figure 16. Spatial variations of upward radiation fluxes (PAR, NIR, and TIR) and net radiation at three different heights (1 m: understory level, 12m: above the canopy, 23 m: eddy covariance tower height). The size of area is 100 by100 m and the eddy covariance tower is located at the center of the images. Spatial averages (Avg.) and standard deviations (STD) are also shown (unit: W m-^{2}). Simulation was performed at 12:00 PM, DOY115, 2008. The small blue dots on the TIR image at 1m level are the position of stem.